Linear stability analysis of magnetized relativistic jets: the non-rotating case

G. Bodo,[1]* G. Mamatsashvili,[2] P. Rossi[1] and A. Mignone[3]

[1]*INAF/Osservatorio Astronomico di Torino, Strada Osservatorio 20, I-10025 Pino Torinese, Italy*
[2]*Department of Physics, Faculty of Exact and Natural Sciences, Tbilisi State University, Il. Chavchavadze ave. 3, Tbilisi 0179, Georgia*
[3]*Dipartimento di Fisica Generale 'Amedeo Avogadro' Università degli Studi di Torino, Via Pietro Giuria 1, I-10125 Torino, Italy*

ABSTRACT

We perform a linear analysis of the stability of a magnetized relativistic non-rotating cylindrical flow in the approximation of zero thermal pressure, considering only the $|m| = 1$ mode. We find that there are two modes of instability: Kelvin–Helmholtz and current driven. The Kelvin–Helmholtz mode is found at low magnetizations and its growth rate depends very weakly on the pitch parameter. The current-driven modes are found at high magnetizations and the value of the growth rate and the wavenumber of the maximum increase as we decrease the pitch parameter. In the relativistic regime the current-driven mode is split in two branches, the branch at high wavenumbers is characterized by the eigenfunction concentrated in the jet core; the branch at low wavenumbers is instead characterized by the eigenfunction that extends outside the jet velocity shear region.

Key words: instabilities – MHD – relativistic processes – galaxies: jets.

1 INTRODUCTION

The formation and propagation of astrophysical jets are strongly affected by plasma instabilities, whose study is therefore of fundamental importance for understanding their dynamics and their associated phenomenology. In jets there are several possible different kinds of instability, among them the most studied are the Kelvin–Helmholtz instability (KHI) driven by the velocity shear between the jet and the ambient medium and the current-driven instability (CDI) associated with a longitudinal current and therefore with the toroidal component of magnetic field. Since the most promising models for the acceleration and collimation of jets involve the presence of a magnetic field with footpoints anchored to a rotating object (an accretion disc or a spinning star or black hole), the presence of a toroidal field component is a natural consequence and CDI may play an important role in the jet propagation. Among CDI, the $|m| = 1$ kink mode is the most effective, leading to a helical displacement of the whole jet body, and for this reason is the only one we will consider in this paper. Recent numerical simulations have shown the development of such instabilities both in Newtonian (Nakamura & Meier 2004; Moll, Spruit & Obergaulinger 2008) and in relativistic (McKinney & Blandford 2009; Mignone et al. 2010) jets. An important step towards a better understanding of simula-

tion results is a linear analysis of the instabilities, that is still largely missing for the relativistic magnetohydrodynamic (MHD) regime.

KHI have been extensively studied in several different configurations in the Newtonian (see e.g. Bodo et al. 1989; Birkinshaw 1991; Hardee et al. 1992; Bodo et al. 1996; Hardee 2006) and relativistic (see e.g. Ferrari, Trussoni & Zaninetti 1978; Hardee 1979; Urpin 2002; Perucho et al. 2004, 2010) cases, but very few linear analyses have been presented for a relativistic magnetized jet (Mizuno, Hardee & Nishikawa 2007). Similarly, CDI have been widely studied in the Newtonian limit (see e.g. Appl & Camenzind 1992; Appl 1996; Begelman 1998; Appl, Lery & Baty 2000; Baty & Keppens 2002); however, for the relativistic MHD case, only the force-free limit has been considered (Istomin & Pariev 1994, 1996; Lyubarskii 1999; Tomimatsu, Matsuoka & Takahashi 2001; Narayan, Li & Tchekhovskoy 2009). Istomin & Pariev (1994, 1996) have considered the case in which the longitudinal magnetic field is constant, showing that in this case the jet is stable, on the contrary Lyubarskii (1999) showed that jets with longitudinal magnetic field decreasing outward can be unstable. Tomimatsu et al. (2001) finally derived a general necessary condition for instability.

The force-free limit is valid when the energy density of electromagnetic fields is much larger than the energy density of matter, i.e. when the jet energy flux is mainly in the form of Poynting flux. Acceleration models predict that jets start being Poynting dominated and progressively undergo a transition to a matter-dominated state, but how fast the transition occurs is uncertain. From the observational point of view, the evidence is that, above the parsec scale, jets

*E-mail: bodo@oato.inaf.it

cannot be Poynting dominated (Sikora et al. 2005; Celotti & Ghisellini 2008). On the other hand, it has been suggested (Sikora et al. 2005) that jet instabilities may play a role in this conversion and that blazar activity could be linked to the development of such instabilities either through shock formation or through direct magnetic energy dissipation processes. These considerations suggest that it is very important to go beyond the force-free limit in the instability analysis and this is exactly the aim of the present paper in which we will analyse the linear stability properties of a cylindrical magnetized relativistic flow, taking into account the effects of matter inertia, but still neglecting thermal pressure. Since the equilibrium configurations of the jet may be quite complex, with many possible sources of instabilities, like the longitudinal jet velocity, the toroidal field and the jet rotation, we will not start from a full configuration where all the above elements are present, but from a simpler case where one of the above elements, namely rotation, is absent. The additional effects introduced by rotation will then be examined in a following paper. In Section 2 we will describe the physical problem, the relevant equations, and the general equilibrium configuration, while in Section 3 we will derive the linearized equations and describe the procedure for finding the normal modes. In Section 4 we will present the results of our analysis for the non-rotating case, first for a static configuration and then for a moving jet. Finally in Section 5 we will summarize our findings.

2 PROBLEM DESCRIPTION

We study the stability of a cold (zero pressure) relativistic magnetized cylindrical flow. The relevant equations are continuity and momentum coupled with Maxwell equations:

$$\frac{\partial}{\partial t}(\gamma \rho) + \nabla \cdot (\gamma \rho \boldsymbol{v}) = 0 \,, \tag{1}$$

$$\gamma \rho \frac{\partial}{\partial t}(\gamma \boldsymbol{v}) + \gamma \rho (\boldsymbol{v} \cdot \nabla)(\gamma \boldsymbol{v}) = \boldsymbol{J} \times \boldsymbol{B} + \frac{(\nabla \cdot \boldsymbol{E})\boldsymbol{E}}{4\pi} \,, \tag{2}$$

$$\frac{\partial \boldsymbol{B}}{\partial t} = -\nabla \times \boldsymbol{E} \,, \tag{3}$$

$$\frac{\partial \boldsymbol{E}}{\partial t} = \nabla \times \boldsymbol{B} - 4\pi \boldsymbol{J} \,, \tag{4}$$

where ρ is the proper density, γ is the Lorentz factor, and $\boldsymbol{v}$, $\boldsymbol{B}$, $\boldsymbol{E}$, $\boldsymbol{J}$ are, respectively, the velocity, magnetic field, electric field and current 3-vectors. The units are chosen so that the speed of light is $c = 1$; we also remark that in the following a factor of $\sqrt{4\pi}$ will be reabsorbed in the definitions of $\boldsymbol{E}$ and $\boldsymbol{B}$. The first step in the stability analysis is to define an equilibrium state satisfying the stationary form of equations (1)–(4) and this will be done in the next subsection.

2.1 Equilibrium configuration

We adopt a cylindrical system of coordinates (r, φ, z) (with versors $\boldsymbol{e}_r$, $\boldsymbol{e}_\varphi$, $\boldsymbol{e}_z$) and seek for axisymmetric steady-state solutions for a relativistic magnetized jet, i.e. $\partial_t = \partial_\varphi = \partial_z = 0$. We assume that the jet propagates in the vertical (z) direction and the magnetic field configuration consists of a vertical (poloidal) component B_z and a toroidal component B_φ and can be expressed as

$$\boldsymbol{B} = B_\varphi(r)\boldsymbol{e}_\varphi + B_z(r)\boldsymbol{e}_z \,. \tag{5}$$

The magnetic field configuration can be characterized by the pitch parameter

$$P = \frac{r B_z}{B_\varphi} \,. \tag{6}$$

From the stationarity condition, the continuity equation and the independence of v_r on z and φ, we get $v_r = 0$; we obtain that the velocity can then be written as

$$\boldsymbol{v} = v_z(r)\boldsymbol{e}_z + v_\varphi(r)\boldsymbol{e}_\varphi = \kappa(r)\boldsymbol{B} + \Omega(r)r\boldsymbol{e}_\varphi \,, \tag{7}$$

where v_φ is the fluid toroidal velocity and Ω is the angular velocity of field lines and they are related by

$$\Omega = \frac{v_\varphi}{r} - \frac{v_z B_\varphi}{r B_z} = \frac{v_\varphi}{r} - \frac{v_z}{P} \,. \tag{8}$$

The electric field is always directed radially and can be expressed as

$$\boldsymbol{E} = -\Omega r B_z \boldsymbol{e}_r \,. \tag{9}$$

The only remaining non-trivial equation is given by the radial component of the momentum equation (2) which simplifies to

$$\rho \gamma^2 v_\varphi^2 = \frac{1}{2r}\frac{\mathrm{d}(r^2 H^2)}{\mathrm{d}r} + \frac{r}{2}\frac{\mathrm{d}B_z^2}{\mathrm{d}r} \,, \tag{10}$$

where $H^2 = B_\varphi^2 - E_r^2$. In the non-relativistic limit H reduces to B_φ and the equilibrium condition acquires the classical Newtonian form

$$\rho v_\varphi^2 = \frac{1}{2r}\frac{\mathrm{d}\left(r^2 B_\varphi^2\right)}{\mathrm{d}r} + \frac{r}{2}\frac{\mathrm{d}B_z^2}{\mathrm{d}r} \,. \tag{11}$$

Equations (10) or (11) leave the freedom of choosing the radial profiles of all flow variables but one and then solve for the remaining profile. We begin by prescribing the profiles of the proper density and Lorentz factor that well describe a jet configuration, with the velocity and density variations concentrated inside the jet radius r_j

$$\rho(r) = \eta + \frac{1-\eta}{\cosh(r/r_\mathrm{j})^6} \,, \tag{12}$$

$$\gamma_z(r) = 1 + \frac{\gamma_c - 1}{\cosh(r/r_\mathrm{j})^6} \,, \tag{13}$$

where η is the ambient/jet density contrast, $\gamma_z(r)$ is the Lorentz factor relative to the z component of the velocity only, while $\gamma_c = 1/\sqrt{1 - v_c^2}$ is the Lorentz factor on the axis where the vertical flow velocity is $v_z(0) = v_c$. From now on, we will use the subscript c to denote values at $r = 0$.

We note that, in the Newtonian case, the presence of a longitudinal velocity has no effect on the radial equilibrium equation (11), while it changes the relativistic equation (10) modifying the centrifugal term.

In the Newtonian limit, it is then customary to prescribe the profile of the azimuthal field B_φ and this choice is more arbitrary since we have no direct information about the magnetic configuration in astrophysical jets. The choice of the B_φ distribution is equivalent to a choice of the distribution of the longitudinal component of the current and also determines the behaviour of the pitch parameter $P(r)$, that is important for the stability properties. In principle, one can then have several equilibria characterized by different forms of the current distribution, that can be more or less concentrated, can peak on the axis or at the jet boundary, and can close in different

ways (see e.g. Appl et al. 2000; Bonanno & Urpin 2008, 2011). In this limit, we start by considering the azimuthal field profile

$$B_\varphi^2 = \frac{B_{\varphi c}^2}{(r/r_j)^2} \left[1 - \exp\left(-\frac{r^4}{a^4}\right) \right],$$ (14)

where a is the magnetization radius and $B_{\varphi c}$ determines the maximum field strength. This profile corresponds to a current distribution peaked on the jet axis and, choosing $a < r_j$, concentrated inside the jet. In addition, one can assume that the current closes at very large distances from the jet. In the relativistic limit the most natural generalization is to prescribe in a similar way the behaviour of H

$$H^2 = \frac{H_c^2}{(r/r_j)^2} \left[1 - \exp\left(-\frac{r^4}{a^4}\right) \right].$$ (15)

We observe that, in the absence of rotation, H represents the azimuthal field strength measured in the proper frame. Prescribing the profile of H instead of B_φ modifies the current profile in the laboratory frame, introducing a return current in the region of the velocity shear and this has consequences for the stability properties as it will be discussed below.

Furthermore, the equilibrium configuration may be modified by the presence of rotations to different degrees: in one extreme case the gradient of $r^2 H^2$ in equation (10) [or the gradient of $r^2 B_\varphi^2$ in equation (11)] is exactly balanced by the centrifugal force and B_z is constant, in the other extreme it is balanced by the gradient of B_z^2. This suggests to introduce, more generally, a parameter $\alpha \in [0, 1]$ so that the equilibrium poloidal magnetic field is given by

$$B_z^2 = B_{zc}^2 - (1 - \alpha) \frac{H_c^2 \sqrt{\pi}}{(a/r_j)^2} \operatorname{erf}\left(\frac{r^2}{a^2}\right)$$ (16)

where erf is the error function, $\alpha = 0$ corresponds to the absence of rotation, while $\alpha = 1$ corresponds to maximum rotation. Introducing the expression for B_z given by equation (16) in equation (10) we can get the azimuthal velocity from

$$2\rho\gamma^2 v_\varphi^2 = \frac{\alpha}{r} \frac{\mathrm{d}(r^2 H^2)}{\mathrm{d}r}.$$ (17)

Finally, the azimuthal field is obtained from the definition of H^2 using $E_r = -(v_\varphi B_z - v_z B_\varphi)$. This yields a quadratic equation in B_φ with solution

$$B_\varphi = \frac{-v_\varphi v_z B_z \mp \sqrt{v_\varphi^2 B_z^2 + H^2 \left(1 - v_z^2\right)}}{1 - v_z^2}.$$ (18)

Here we consider the negative branch because it guarantees that B_φ and v_φ have opposite signs, as suggested by acceleration models. Thus, in our model the radial profile of the pitch parameter, equation (6), is always negative. We choose to control the magnetic field configuration by specifying the value of the pitch on the axis P_c and the ratio between the energy density of the matter and the magnetic energy density M_a^2, where

$$P_c \equiv \left| \frac{r B_z}{B_\varphi} \right|_{r=0}, \qquad M_a^2 \equiv \frac{\left(\rho \gamma_c^2\right)}{\langle \boldsymbol{B}^2 \rangle},$$ (19)

and $\langle \boldsymbol{B}^2 \rangle$ represents the average across the beam:

$$\langle \boldsymbol{B}^2 \rangle = \frac{\int_0^{r_j} \left(B_z^2 + B_\varphi^2\right) r \, \mathrm{d}r}{\int_0^{r_j} r \, \mathrm{d}r}.$$ (20)

We note that $P_c > 0$ by construction although the radial profile of the pitch parameter (equation 6) using the negative branch of equation (18) in the definition of B_φ is always negative. The constants

B_{zc}^2 and H_c^2 appearing in the above equations can be found in terms of P_c and M_a from the simultaneous solution of the two expressions given in equation (19), together with (20). In particular, from the definition of the pitch parameter, after some algebra we find (in the $r \to 0$ limit)

$$a^4 B_{zc}^2 = \frac{H_c^2 P_c^2}{1 - (H_c P_c \sqrt{\zeta} - v_z)^2}$$ (21)

where $\zeta = 2\alpha/(\gamma_c^2 \rho a^4)$. In practice, equation (21) is used to compute B_{zc}^2 for trial values of H_c^2 until the prescribed value of magnetic energy is satisfied.

Summarizing, our equilibrium configuration depends on the five parameters η, γ_c, α, P_c and M_a^2 specifying, respectively, the jet density contrast, bulk flow velocity, strength of centrifugal force, magnetic pitch and the ratio between the energy density of the matter and the magnetic energy density.

3 LINEARIZED EQUATIONS

Let us consider small perturbations ρ_1, $\boldsymbol{v}_1$, $\boldsymbol{B}_1$, $\boldsymbol{E}_1$ to the equilibrium state described above, which hereafter will be identified by a zero subscript. The linearized continuity, momentum, induction equations and the ideal MHD conditions are

$$\frac{\partial}{\partial t}(\gamma_0 \rho_1 + \gamma_1 \rho_0) + \nabla \cdot (\gamma_0 \boldsymbol{v}_0 \rho_1 + \gamma_1 \boldsymbol{v}_0 \rho_0 + \gamma_0 \rho_0 \boldsymbol{v}_1) = 0,$$ (22)

$$\rho_0 \gamma_0 \left(\frac{\partial}{\partial t} + \boldsymbol{v}_0 \cdot \nabla\right)(\gamma_1 \boldsymbol{v}_0 + \gamma_0 \boldsymbol{v}_1) + \rho_0(\gamma_1 \boldsymbol{v}_0 + \gamma_0 \boldsymbol{v}_1) \cdot \nabla(\gamma_0 \boldsymbol{v}_0)$$

$$+ \rho_1 \gamma_0 \boldsymbol{v}_0 \cdot \nabla(\gamma_0 \boldsymbol{v}_0) = (\nabla \times \boldsymbol{B}_0) \times \boldsymbol{B}_1 + (\nabla \times \boldsymbol{B}_1) \times \boldsymbol{B}_0$$

$$+ \boldsymbol{B}_0 \times \frac{\partial \boldsymbol{E}_1}{\partial t} + \boldsymbol{E}_1(\nabla \cdot \boldsymbol{E}_0) + \boldsymbol{E}_0(\nabla \cdot \boldsymbol{E}_1),$$ (23)

$$\frac{\partial \boldsymbol{B}_1}{\partial t} = -\nabla \times \boldsymbol{E}_1,$$ (24)

$$\boldsymbol{E}_1 = -\boldsymbol{v}_1 \times \boldsymbol{B}_0 - \boldsymbol{v}_0 \times \boldsymbol{B}_1.$$ (25)

Assuming now the perturbations to be of the form $\propto \exp(i\omega t - im\varphi - ikz)$, after lengthy algebraic manipulations described in Appendix A, we arrive at a system of two first order differential equations in the radial coordinate for the two basic variables – the radial displacement ξ_{1r} and the perturbed electromagnetic pressure Π_1 defined as

$$\xi_{1r} = -iv_{1r}/\tilde{\omega},$$ (26)

and

$$\Pi_1 = \boldsymbol{B}_0 \cdot \boldsymbol{B}_1 - \boldsymbol{E}_0 \cdot \boldsymbol{E}_1 = B_{0\varphi} B_{1\varphi} + B_{0z} B_{1z} - E_{0r} E_{1r}.$$ (27)

The system of equations can then be written as

$$D \frac{\mathrm{d}\xi_{1r}}{\mathrm{d}r} = \left(C_1 + \frac{C_2 - Dk_B'}{k_B} - \frac{D}{r}\right) \xi_{1r} - C_3 \Pi_1$$ (28)

$$D \frac{\mathrm{d}\Pi_1}{\mathrm{d}r} = \left[A_1 D - \frac{\rho_0 \gamma_0^2 v_{0\varphi}^2}{r} \left(C_1 + \frac{C_2 - Dk_B'}{k_B} + \frac{C_4}{r} + C_5\right)\right] \xi_{1r}$$

$$+ \left[\frac{1}{r}\left(\rho_0 \gamma_0^2 v_{0\varphi}^2 C_3 - 2D + \frac{C_6}{r} + C_7\right)\right] \Pi_1$$ (29)

where

$$D = (\sigma + 1)B_0^2 \tilde{\omega}^2 + \sigma k_B \left[2\tilde{\omega}(\boldsymbol{v}_0 \cdot \boldsymbol{B}_0) - \frac{k_B}{\gamma_0^2} \right] , \qquad (30)$$

$$\sigma = \frac{B_0^2}{\rho_0 \gamma_0^2}, \qquad \tilde{\omega} \equiv \omega - \frac{m}{r} v_{0\varphi} - k v_{0z}, \qquad k_B \equiv \frac{m}{r} B_{0\varphi} + k B_{0z} . \qquad (31)$$

The quantities A_1, C_1, C_2, C_3, C_4, C_5, C_6, C_7 depend on the chosen profiles of the equilibrium solution and are given in Appendix B. These two equations together with the appropriate boundary conditions represent an eigenvalue problem, where ω is the eigenvalue (we observe that we here adopt a temporal approach to the stability analysis). We have instability when ω has a negative imaginary part.

The domain of integration for equations (28) and (29) covers the interval from 0 to ∞, so we have to specify the boundary conditions at $r = 0$ and for $r \to \infty$. On the axis at $r = 0$ the equations are singular but the solutions have to be regular while at infinity the solutions have to decay and no incoming wave is allowed (Sommerfeld condition). For finding the eigenvalue we use a shooting method with a complex secant root finder. The numerical integration cannot start at $r = 0$ (because of the singularity), so we start at a small distance from the origin where the solution is obtained through a series expansion of the equations described in Appendix C. Similarly, we start a backward integration from a sufficiently large radius, where the asymptotic solution is obtained as described in Appendix D and then we match the two numerical solutions at an intermediate radius. Furthermore, we have to consider that equations (28) and (29) may have singular points, that arise in the following cases:

(i) when the Doppler shifted frequency, $\tilde{\omega}$, appearing in the denominators in A_1 and A_2, becomes zero at some $r = r_c$, $\tilde{\omega}(r_c) = 0$. This is a well-known corotation singularity, when the phase speed of a wave perturbation coincides with the basic flow velocity at $r = r_c$ and corresponds to resonant interaction between waves and the background jet flow. This corotation singularity is a physical one.

(ii) when the determinant becomes zero at some $r = r_A$, $D(r_A) = 0$. The latter condition is a quadratic equation with respect to $\tilde{\omega}$ that gives

$$\tilde{\omega} = \frac{k_B}{\gamma_0^2} \cdot \frac{1}{(\boldsymbol{v}_0 \cdot \boldsymbol{B}_0) \pm \sqrt{(\boldsymbol{v}_0 \cdot \boldsymbol{B}_0)^2 + \frac{B_0^2 + \rho_0 \gamma_0^2}{\gamma_0^2}}} , \qquad (32)$$

from which we derive a phase speed equal to that of a relativistic Alfvén wave as it is given by equation 28 of Keppens & Meliani (2008) and by Istomin & Pariev (1996).

$$v_{\mathrm{ph}} = \hat{\boldsymbol{n}} \cdot \boldsymbol{v}_0 + \frac{\hat{\boldsymbol{n}} \cdot \boldsymbol{B}_0}{\gamma_0^2} \frac{1}{(\boldsymbol{v}_0 \cdot \boldsymbol{B}_0) \pm \sqrt{\rho_0 + 2 p_{\mathrm{mag}}}} , \qquad (33)$$

where $\hat{\boldsymbol{n}} = (k^2 + m^2/r^2)^{-1}(m/r, k)$ is the versor of the wave vector and

$$p_{\mathrm{mag}} = \frac{B_0^2}{\gamma_0^2} + (\boldsymbol{v}_0 \cdot \boldsymbol{B}_0)^2 \qquad (34)$$

is the total pressure. In other words, the above determinant is zero and therefore equations (28) and (29) have singular, or resonant points at $r = r_A$, where the phase speed of the wave perturbation coincides with that of relativistic Alfvén waves. Like the corotation

singularity, this singularity is also physical, and results from the resonant interaction of perturbations with relativistic Alfvén waves.

Istomin & Pariev (1996) have discussed the proper way to handle these singularities, however, since singular points are found only for real values of ω and since we are interested in unstable modes and therefore complex values of ω, we can assume that our integration will always avoid singular points.

4 RESULTS

Before discussing in detail our results, we recall in Section 4.1 the units we will use, the full set of parameters defining our problem and which ones will be investigated in more detail in the present work. We then preliminarily examine the static case in Section 4.2, the full case in Section 4.3, and finally a more detailed analysis of the CDI is performed in Section 4.4.

4.1 Parameters and units

As discussed in Section 2.1, the basic equilibrium state is determined by five parameters: the jet density contrast η, the bulk flow velocity which is derived from γ_c, the rotation parameter α, the pitch on the axis P_c and the ratio M_a^2 between the energy density of the matter and the magnetic energy density. We notice that our parameter M_a^2 is the inverse of the magnetization parameter often used in the literature. In the present paper, as already discussed, we consider
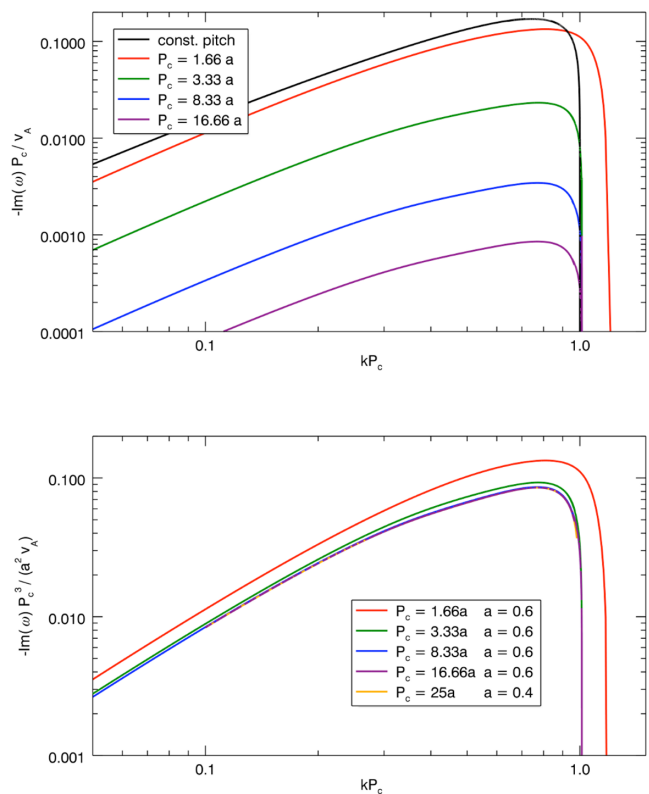
Figure 1. Normalized plots of the growth rate as a function of the wavenumber for a static column and for different values of the pitch parameter P_c. The values of P_c for the different curves are reported in the legend and, for comparison, in the top panel, we plot also the case of a configuration with constant pitch. In the bottom panel we show how well the scaling given by equation (36) reproduces our results, a significant deviation can be observed only for $P_c/a = 1.66$.
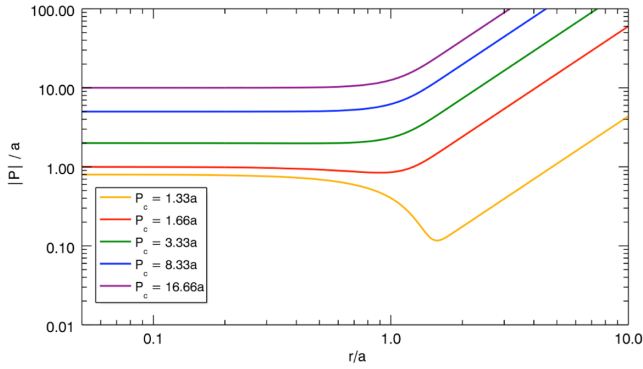
Figure 2. Plot of the pitch profile as a function of r/a. The different curves refer to different values of the parameter P_c/a, whose values are reported in the legend.

only the case without rotation, so α is kept fixed to 0, and we also consider jets with density equal to that of the ambient medium, so η is kept fixed to 1. We focus our analysis on the dependence on the three parameters γ_c, P_c and M_a. In the following discussion, instead of M_a we will make use of the quantity $M_a v_c$ which, in the Newtonian limit, corresponds to the ratio between the jet speed and the Alfvén speed, while in the relativistic limit reduces to M_a. The unit of velocity is the light speed c and we choose as unit of length the jet radius r_j, so, unless otherwise specified, the growth rate is expressed in units of c/r_j. An additional parameter is represented by the width a of the current distribution, this parameter, unless otherwise specified, is kept fixed to $a = 0.6$. Of course, in the static case, the jet radius has no significance and is an arbitrary measure; however we keep it as the unit of length for consistency with the general case.

4.2 The static case, $v_z = 0$

Static columns in the Newtonian case have been already studied by many authors (see e.g. Appl et al. 2000; Bonanno & Urpin

2008, 2011) and differ one another in many respects, but mainly for the parameter range considered and for the equilibrium magnetic field configuration. In particular the studies by Bonanno & Urpin (2008) consider cases with subthermal magnetic field strength. In the present work, conversely, we neglect the pressure term and our regime of investigation addresses the case of suprathermal field strengths and can be compared with that of Appl et al. (2000), that is performed in the same regime.

In the study of CDI, a very important role is played by resonant surfaces, i.e. the surfaces where the condition $\boldsymbol{k} \cdot \boldsymbol{B} = 0$ is satisfied. On these surfaces, in fact, the stabilizing effect of magnetic tension is absent and these regions are therefore more prone to instability. The resonant condition can be rewritten as

$$\boldsymbol{k} \cdot \boldsymbol{B} = kB_z + \frac{m}{r}B_\phi = kP + m = 0. \tag{35}$$

This condition can be verified only for positive m and, for a constant pitch distribution like that used by Appl et al. (2000), marks the stability boundary: wavenumbers larger than this critical limit are stable, while smaller wavenumbers are unstable. This behaviour can be observed in the top panel of Fig. 1, where we plot the growth rate as a function of the wavenumber for the case with $m = 1$ for the constant pitch configuration (black curve, top panel) and for our equilibrium model (coloured lines). In the top panel we measure the wavenumber in units of $1/P_c$ and the growth rate in units of v_A/P_c. In these units, the constant pitch solutions of Appl et al. (2000) are all represented by the single black curve independently of the pitch value. Instability is present for all wavenumbers $k < 1/P_c$ (i.e. for wavenumbers lower than the threshold given by the resonance condition equation 35) and, for $k \to 0$, the growth rate decreases as a power law. We note that, while we employ radiation condition at infinity, Appl et al. (2000) in most of their calculations made use of boundary conditions consistent with a rigid wall set at a finite radial distance. This condition introduces a new scale and restricts the unstable range in wavenumbers, with a small wavenumber cut-off. Our equilibria are characterized by two length scales: the pitch value on the axis P_c and the width of the current distribution a and therefore we have the additional parameter P_c/a. The pitch profile
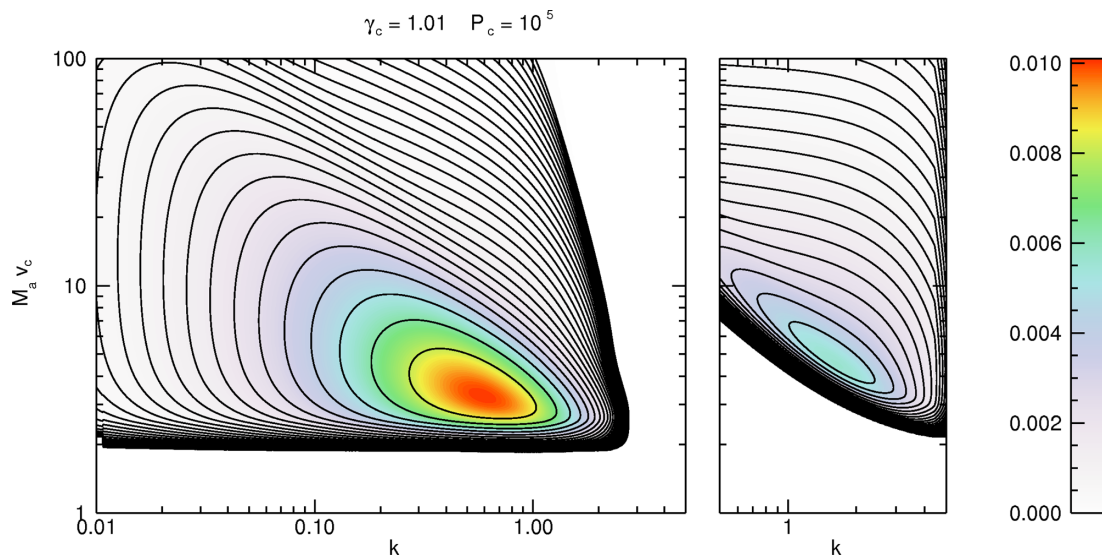
Figure 3. Distribution of the growth rate as a function of the wavenumber and of $M_a v_c$ for the case with $\gamma_c = 1.01$ and $P_c = 10^5$. As discussed in the text, the results for the two cases $m = 1$ and $m = -1$ coincide. In the left-hand panel we have the KH ordinary mode, while in the right-hand panel we have the first reflected KH mode. The levels are equispaced in logarithmic scale from 10^{-5} to the maximum value of the growth rate.
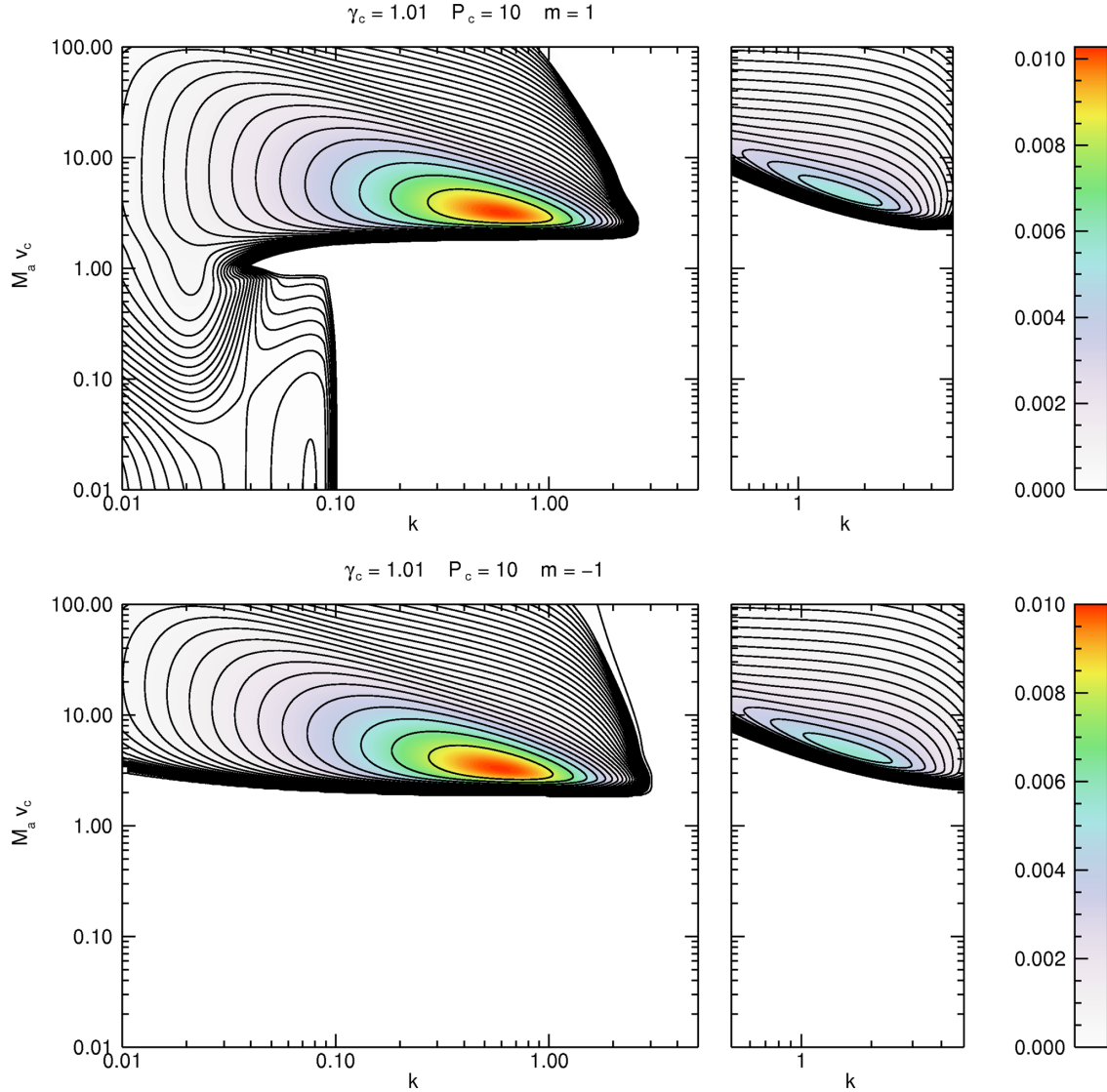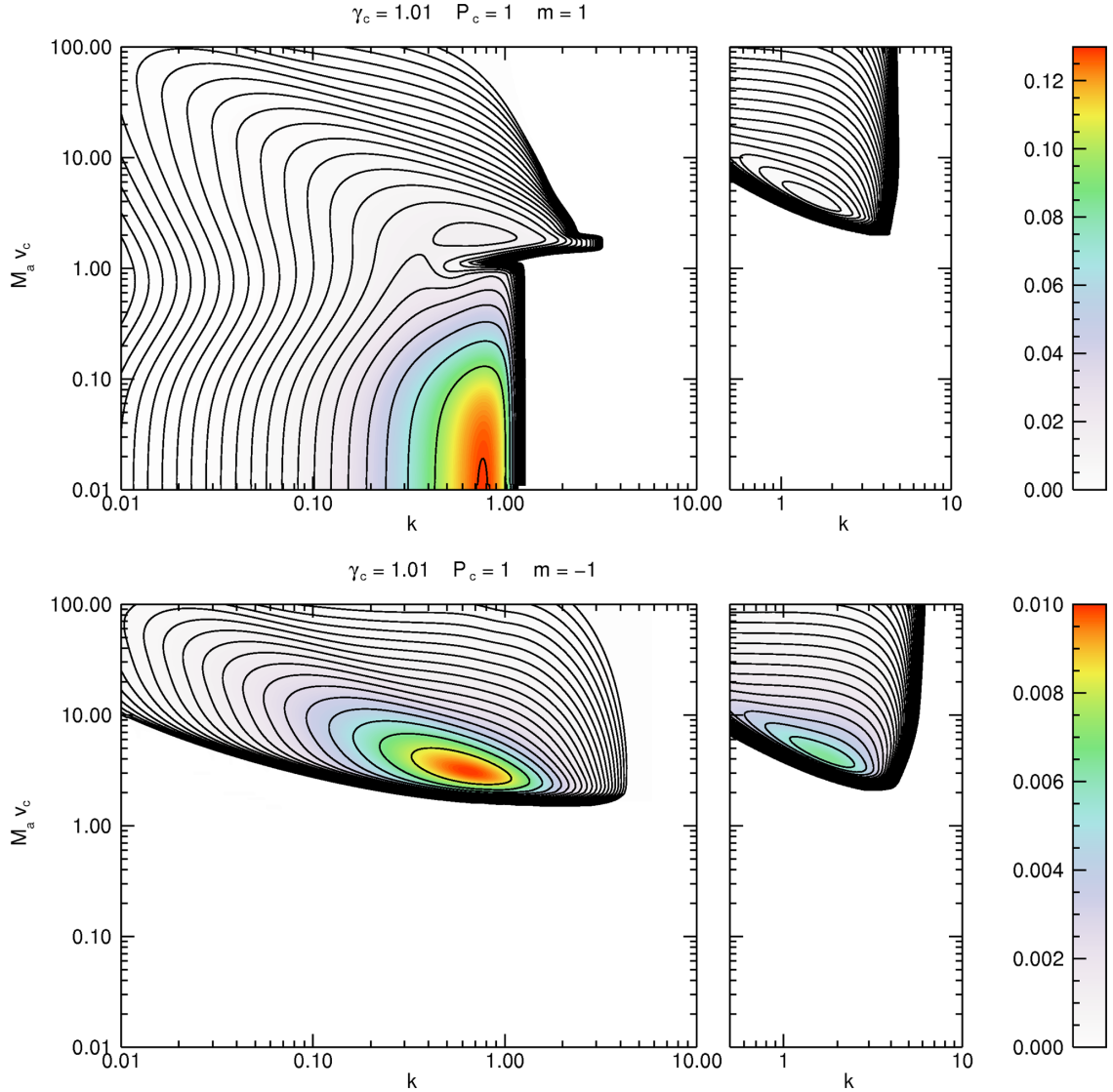
Figure 4. Distribution of the growth rate as a function of the wavenumber and of $M_a v_c$ for the case with $\gamma_c = 1.01$ and $P_c = 10$. The top panels refer to $m = 1$ while the bottom panels refer to $m = -1$. In the left panels, for high values of $M_a v_c$, we have the ordinary mode of the KH instability, for low values of $M_a v_c$ the case $m = 1$ (top) shows the CDI, while the case $m = -1$ (bottom) is stable. In the right panels, we have the first reflected KH mode. The levels are equispaced in logarithmic scale from 10^{-5} to the maximum value of the growth rate.

$P(r)$ plays a fundamental role for the stability properties and, for our equilibrium configurations, it is shown in Fig. 2 for different values of P_c/a. It is always characterized by an increase at large radii, owing to the confinement of the current inside $r < a$, while in the central region we can distinguish two regimes: for $P_c/a \gg 1$ the pitch is constant up to $r/a = 1$ while for $P_c/a \sim 1$ it decreases to a minimum value at $r/a \sim 1.5$ immediately after the inner flat region. Furthermore, there exists a critical value of $P_c/a = 1.33$ below which equilibrium configurations are not possible. Below this critical value, the equilibrium condition would require a negative value of B_z^2 meaning that the longitudinal field pressure gradient is no longer able to balance the inward force of the azimuthal magnetic field. The behaviour of the growth rate in the first regime ($P_c/a \gg 1$) has a form similar to the constant pitch situation, but its value decreases as the parameter P_c/a increases, as it is shown in the top panel of Fig. 1. In the same limit the growth rate takes the asymptotic

form

$$\mathrm{Im}(\omega) \sim \frac{v_A}{P_c} \left(\frac{a}{P_c}\right)^2 f(k P_c), \tag{36}$$

where the function $f(k P_c)$ is independent from P_c/a. The validity of the previous scaling law for any value of P_c/a is demonstrated in the bottom panel of Fig. 1, where we plot $\mathrm{Im}(\omega) P_c^3/a^2 v_A$ as a function of $k P_c$. The curves in the figures, therefore, represent the function $f(k P_c)$ and should be independent from P_c/a. In fact, the purple ($P_c/a = 16.66$, $a = 0.6$), blue ($P_c/a = 8.33$, $a = 0.6$) and orange ($P_c/a = 25$, $a = 0.4$) curves are overimposed and almost coincident with the green curve corresponding to $P_c/a = 2.66$, $a = 0.6$. A significant deviation from the above scaling is observed only for $P_c/a = 1.66$, as shown by the red curve. In this case, as discussed above, we have a region of decreasing pitch whose effect is to widen the instability range to larger values of $k P_c$ thus

Figure 5. Distribution of the growth rate as a function of the wavenumber and of $M_a v_c$ for the case with $\gamma_c = 1.01$ and $P_c = 1$. The top panels refer to $m = 1$ while the bottom panels refer to $m = -1$. In the left panels, for high values of $M_a v_c$, we have the ordinary mode of the KH instability, for low values of $M_a v_c$ the case $m = 1$ (top) shows the CDI, while the case $m = -1$ (bottom) is stable. In the right panels we have the first reflected KH mode. The levels are equispaced in logarithmic scale from 10^{-5} to the maximum value of the growth rate.

increasing the growth rate above the value predicted by the scaling law and moving the maximum towards somewhat larger values of kP_c.

For a static configuration, relativistic effects are introduced only by increasing the magnetic field strength and the previous results shown in Fig. 1 remain the same provided the Alfvén velocity is replaced by the correct relativistic expression

$$v_A = \frac{|\boldsymbol{B}|}{\sqrt{w + \boldsymbol{B}^2}}, \tag{37}$$

where w is the gas enthalpy.

4.3 The case with $v_z \neq 0$

We start the discussion of the dynamic case considering a flow moving at $\gamma_c = 1.01$, corresponding to a non-relativistic $v_c \sim 0.14$. In this case the results obtained in the Newtonian limit coincide al-

most exactly with those obtained with the full relativistic treatment. An overview of the mode structure can be gained by looking at Figs 3–5, where we show the behaviour of the growth rate as a function of the wavenumber k and of $M_a v_c$ for $P_c = 10^5$, $P_c = 10$ and $P_c = 1$, respectively. Figs 4 and 5 present the results for $m = 1$ in the upper panels and for $m = -1$ in the lower panels, while in Fig. 3 the system has no way to distinguish between $m = 1$ and $m = -1$ and the results for the two modes are coincident. As mentioned, we now expect the appearance of two types of instability, namely, KHI and CDI. Moreover, in the case of a purely longitudinal field, CDI are absent and only KHI may be effective. This is the case of Fig. 3, where we show the results for $P_c = 10^5$, i.e. for a magnetic field almost exactly longitudinal. The two panels in the figure refer to the ordinary mode and to the first reflected mode (for a discussion on reflected modes, see e.g. Bodo et al. 1989). From the figure, we can see that the jet is stable below $M_a v_c \sim v_c/v_A \sim 2$, the maximum growth rate for the ordinary mode is $\mathrm{Im}(\omega_{\max}) \sim 0.01$ and it is found
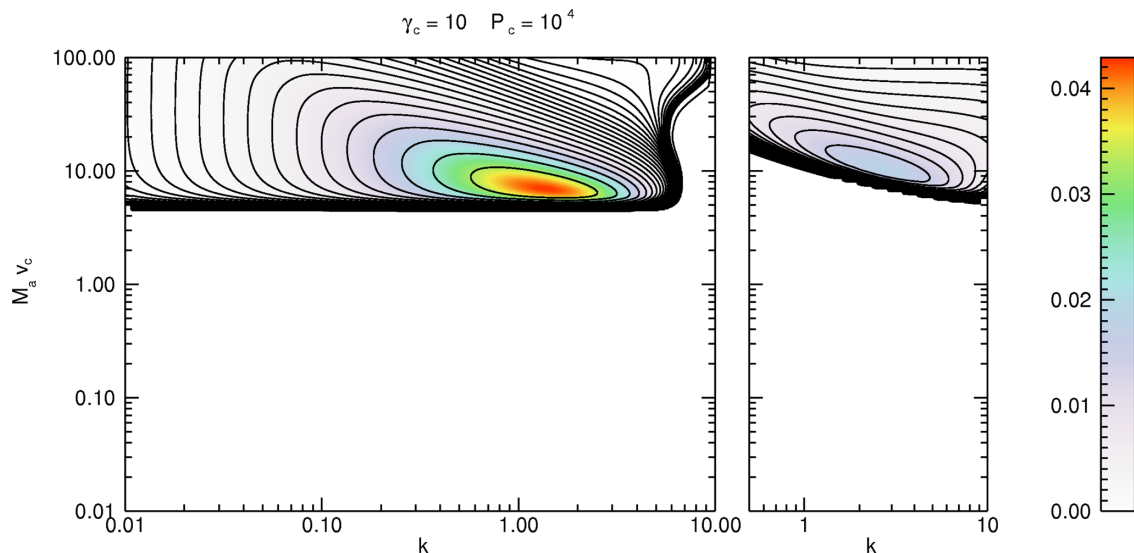
Figure 6. Distribution of the growth rate as a function of the wavenumber and of $M_a v_c$ for the case with $\gamma_c = 10$ and $P_c = 10^4$ (corresponding to $P_c = 10^5$ in the rest frame of the jet). As discussed in the text, the results for the two cases $m = 1$ and $m = -1$ coincide. In the left-hand panel we have the KH ordinary mode, while in the right-hand panel we have the first reflected KH mode. The levels are equispaced in logarithmic scale from 10^{-5} to the maximum value of the growth rate.

at $k \sim 0.6$ and $M_a v_c \sim v_c/v_A \sim 3$. Moving towards higher values of v/v_A, the relative maximum shifts towards smaller values of k and our results show that both the wavenumber of the maximum and the maximum itself scale as v_A/v_c. The first reflected mode (right panel) has a smaller growth rate, $\mathrm{Im}(\omega_{\max}) \sim 0.005$, and remains unstable at larger values of k as expected.

Fig. 4 refers to $P_c = 10$ with the upper and lower panels showing, respectively, the growth rates computed for the $m = 1$ and $m = -1$ modes. Clearly, the upper left panel shows a region of instability for small values of $M_a v_c$ which is completely absent in the lower panel. This instability region corresponds to the onset of CDI modes that become stable for $m = -1$ since the resonance condition (equation 35) cannot be satisfied. For small values of $M_a v_c$, the instability behaviour is very similar to the static case discussed in the previous subsection and its growth rate is two order of magnitude smaller than that of the KHI. The mode becomes stable for $k > 0.1$, which corresponds to the stability limit given by the condition $kP_c = 1$. For larger values of $M_a v_c$ the CD mode merge with the KH mode and shows essentially no difference with respect to the previous case.

The results for $P_c = 1$ are shown in Fig. 5. As expected, the CDI moves towards higher values of k as the stability limit $kP_c = 1$ gives a limiting value of $k = 1$. The growth rate of the CD mode also increases and scales as $1/P_c^3$ as in the static case eventually becoming dominant over the KHI. For $m = -1$ (lower panels) the CDI is absent and the KHI presents only slight differences with the cases at larger values of P_c. Increasing the flow velocity up to Lorentz $\gamma_c = 10$, we show the growth rate behaviour as a function of k and $M_a v_c$ in Figs 6–8 corresponding, respectively, to $P_c = 10^4$, $P_c = 1$ and $P_c = 0.1$. We remark that the pitch in the comoving frame is obtained by multiplying the pitch in the lab frame by γ and therefore the chosen values of P_c in the comoving frame are exactly the same ones used for the classical case. The upper and lower panels in Figs 7 and 8 refer, respectively, to $m = 1$ and $m = -1$. Similarly to the classical case, we do not have any difference between the $m = 1$ and $m = -1$ modes for $P_c = 10^4$ (see Fig. 6). The right-hand panels

in each figure show, as before, the reflected KH mode. The general instability behaviour is quite similar to the classical case and we can easily recognize the KHI region and the CDI region. Focusing on the KHI, we see that the stability boundary and, consequently, the position of the maximum growth rate have moved towards larger values of M_a (see Figs 6 and 7, left and right panels) as it is expected to happen for relativistic flows (Osmanov et al. 2008). Decreasing P_c, the KH instability boundary moves towards smaller values of $M_a v_c$, as it is evident in the lower panels of Fig. 8 corresponding to $m = -1$ and in the right upper panel of the same figure (reflected mode $m = 1$). Indeed, the stabilizing longitudinal component of magnetic field decreases with decreasing P_c. In the upper left panel of Fig. 8 we see that, for $m = 1$, the KHI and CDI have merged. Moreover, for each value of P_c, an increase of $M_a v_c$ leads to a shift of the relative maximum of the growth rate towards smaller values of k (see Figs 6–8) and both the wavenumber of the maximum and the maximum itself scale as $1/M_a v_c$ precisely as in the Newtonian limit. In Fig. 9 we plot the value of the maximum growth rate of the KH mode as a function of $\gamma_c v_c$ for $P_c = 1$ and $m = 1$. This curve can be considered representative for any value of the pitch since, as we have seen, the growth rate of the KHI is only weakly dependent on this parameter. In the Newtonian limit, for small values of $\gamma_c v_c$, the growth rate becomes essentially proportional to v_c, reaches a maximum at $\gamma_c v_c \sim 2$ and then progressively decreases. This result is in agreement with the work of Osmanov et al. (2008) that found that relativistic motion plays a stabilizing role on the growth of the KHI.

4.4 The current-driven mode

The CD mode is present only for $m = 1$ (as in the Newtonian case) and, by lowering P_c, it progressively shifts towards larger values of the wavenumber and increases also its growth rate. Moreover, for $P_c = 1$, we observe a splitting of the CDI in two unstable regions (see the lower half in the top left panel of Fig. 7). This mode splitting can be better understood by inspecting Fig. 10 where we
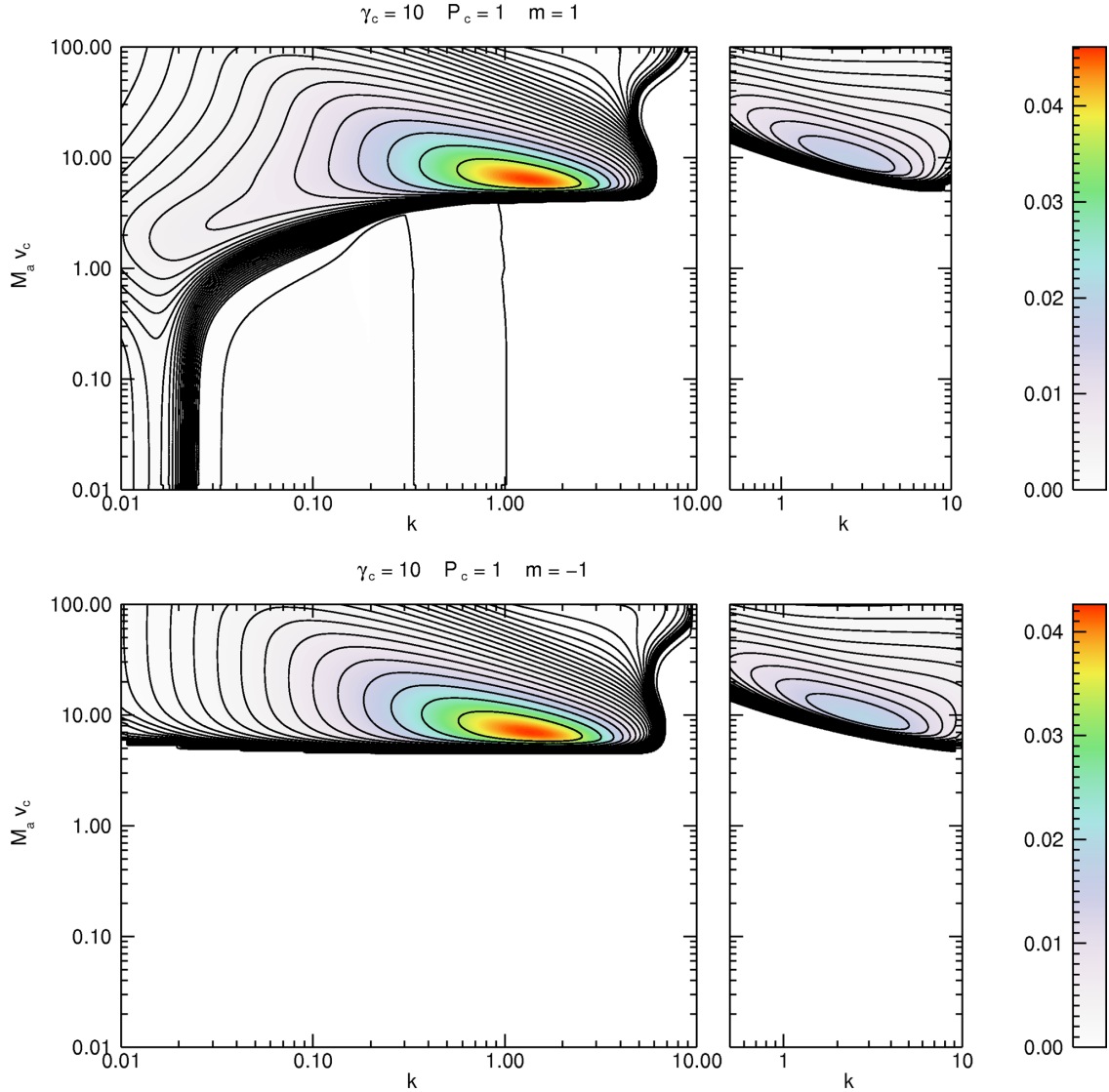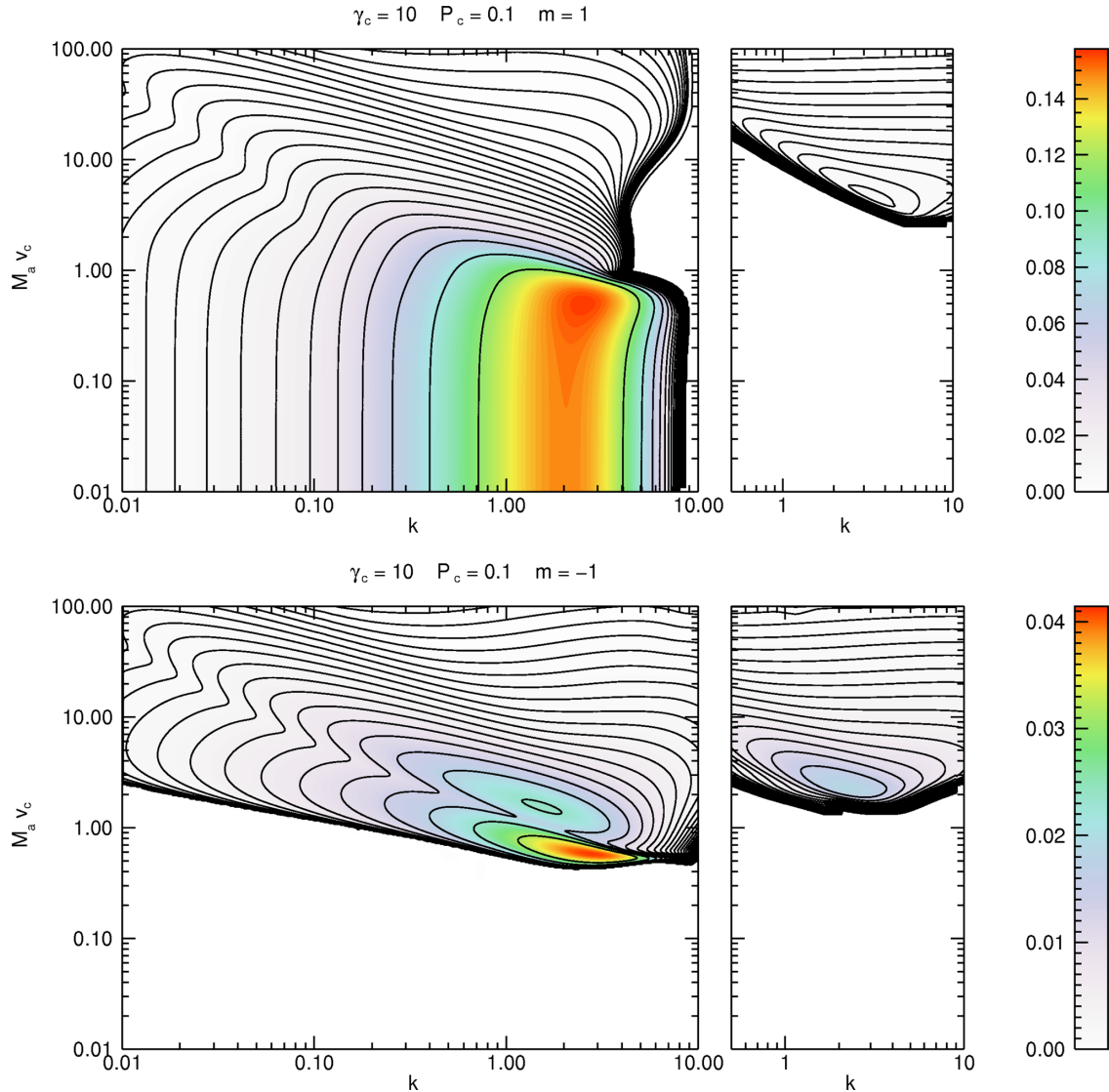
Figure 7. Distribution of the growth rate as function of the wavenumber and of $M_a v_c$ for the case with $\gamma_c = 10$ and $P_c = 1$ (corresponding to $P_c = 10$ in the rest frame of the jet). The top panels refer to $m = 1$ while the bottom panels refer to $m = -1$. In the left-hand panels, for high values of $M_a v_c$, we have the ordinary mode of the KH instability, for low values of $M_a v_c$ the case $m = 1$ (top) shows the CDI which is split in two branches (note that the region between $k = 0.04$ and $k = 0.3$ is stable), while the case $m = -1$ (bottom) is stable. In the right panels we have the first reflected KH mode. The levels are equispaced in logarithmic scale from 10^{-5} to the maximum value of the growth rate.

plot the normalized growth rate as a function of the wavenumber k for $M_a = 0.01$ and different values of P_c. Since for $M_a \lesssim 0.1$ the CDI becomes essentially independent of M_a, the curves plotted in Fig. 10 are representative of the instability behaviour for small values of M_a. The three panels refer to different values of γ_c, namely, $\gamma_c = 1.01$ in the upper panel, $\gamma_c = 2$ in the middle panel and $\gamma_c = 10$ in the lower panel. In the upper panel we see that the behaviour of CDI at small non-relativistic velocities is essentially the same as in the static case (see Fig. 1 for comparison). When γ_c is increased to 2 (middle panel), we observe that the mode splits into two. In order to comprehend the reason behind the observed mode splitting, we plot in Fig. 11 the radial profiles of the Lorentz factor (top panel), pitch (middle panel) and the eigenfunctions relative to the electromagnetic pressure perturbation for two different values of the wavenumber, in the case with $\gamma_c = 2$ and $P_c = 1$ (bottom panel). The red shading marks the shear region where the jet velocity

decreases and pitch profile becomes the steepest. In plotting the eigenfunctions, we have chosen the wavenumbers $k = 0.1$ (blue curve) and $k = 0.8$ (orange curve) which correspond to the maximum growth rate of each of the two branches shown by the green curves in the middle panel of Fig. 10. The modes present a resonant behaviour and the peak positions are located at the radii where the condition $kP(r) = 1$ is fulfilled. Looking at the form of the eigenfunctions in the bottom panel of Fig. 11, we see that the mode with $k = 0.8$ peaks inside the jet core in the flat part of the pitch profile. At the opposite, the mode with $k = 0.1$ reaches a maximum outside the velocity shear region. For this reason, we denote the right branch at large wavenumbers as the 'inner mode' and the left branch at small wavenumbers as the 'outer mode'.

Given that the absolute value of the pitch is monotonically increasing with radius, we note that the resonant position, expressed by the condition $kP(r) = 1$, has to shift to larger radii as k is

Figure 8. Distribution of the growth rate as a function of the wavenumber and of $M_a v_c$ for the case with $\gamma_c = 10$ and $P_c = 0.1$ (corresponding to $P_c = 1$ in the rest frame of the jet). The top panels refer to $m = 1$ while the bottom panels refer to $m = -1$. As discussed in the text, for $m = 1$ (top), the KH ordinary mode and the current-driven mode merged. In the right panel we have the first reflected KH mode. The levels are equispaced in logarithmic scale from 10^{-5} to the maximum value of the growth rate.
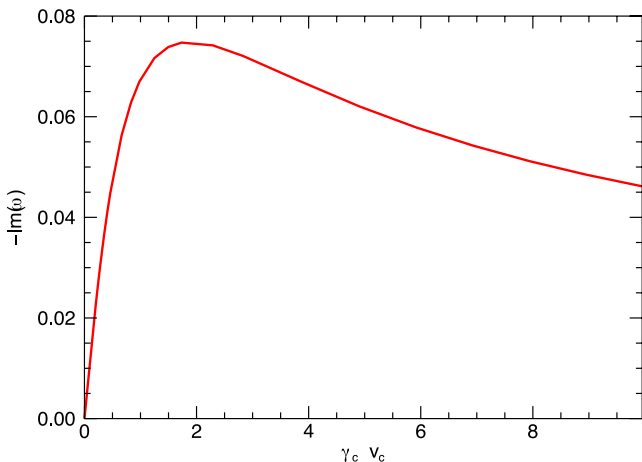
Figure 9. Plot of the maximum growth rate of the KHI as a function of $\gamma_c v_c$ for $P_c = 1$ and $m = 1$.

decreased. Thus, if we focus on the inner mode, the resonant position will move from $r \sim 0$ (at large k) towards the exterior until, for a lower value of k, it will fall inside the shear region where the pitch profile is steeper, thereby becoming stabilized. A further decrease in the wavenumber leads the resonance point outside the velocity shear region, where the pitch slope decreases, thus giving rise to the outer branch of the instability. The outer mode, for the considered parameters, has a growth rate that is always somewhat larger than that of the inner mode and it is the one visible in Fig. 8 (upper left panel).

For smaller values of P_c, Fig. 10 shows that the deviation of the growth rate from the P_c^3 scaling (equation 36) becomes larger and the outer mode stretches while moving towards larger values of k. At the same time, the inner mode widens while moving towards lower values of k, until a region of superposition between the two modes is formed. This behaviour can be attributed to the non-monotonic trend of the pitch for small values of P_c, as already shown in Fig. 2.
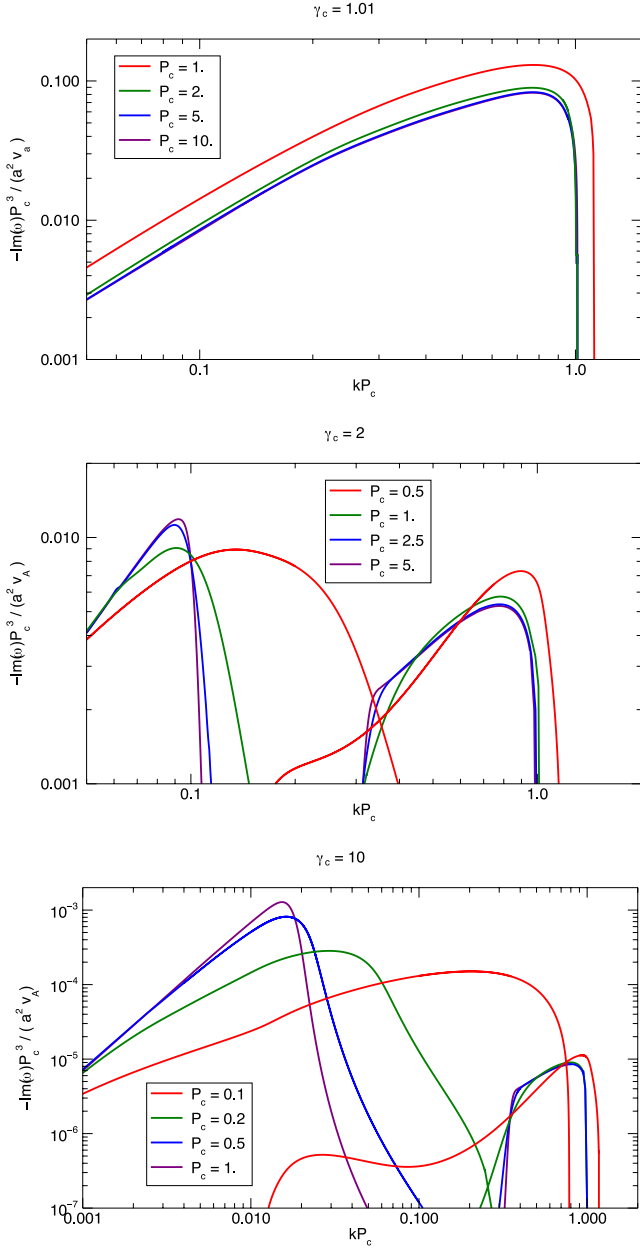
Figure 10. Plots of the (normalized) growth rate as a function of the wavenumber, for the four different values of the pitch parameter P_c given in the legends and for $M_a = 0.01$. The three panels refer to three different values of γ_c, more precisely $\gamma_c = 1.01$ for the top panel, $\gamma_c = 2$ for the middle panel and $\gamma_z = 10$ for the bottom panel. The values of P_c are chosen so that in the rest frame we have always $P'_c = 1, 2, 5, 10$. In the relativistic case we observe the splitting of the mode in two branches as described in the text.

The inner mode, being confined inside the jet core, does not feel the effect of the velocity shear and its properties may be derived by simply applying the appropriate Lorentz transformations to the results obtained in the static case. We can in fact relate the pitch, growth rate and wavenumber in the jet frame to those measured in the laboratory frame by the following relations:

$$P_c = \frac{P'_c}{\gamma_c}, \qquad \mathrm{Im}(\omega) = \frac{\mathrm{Im}(\omega')}{\gamma_c}, \qquad k = k' \gamma_c, \qquad (38)$$
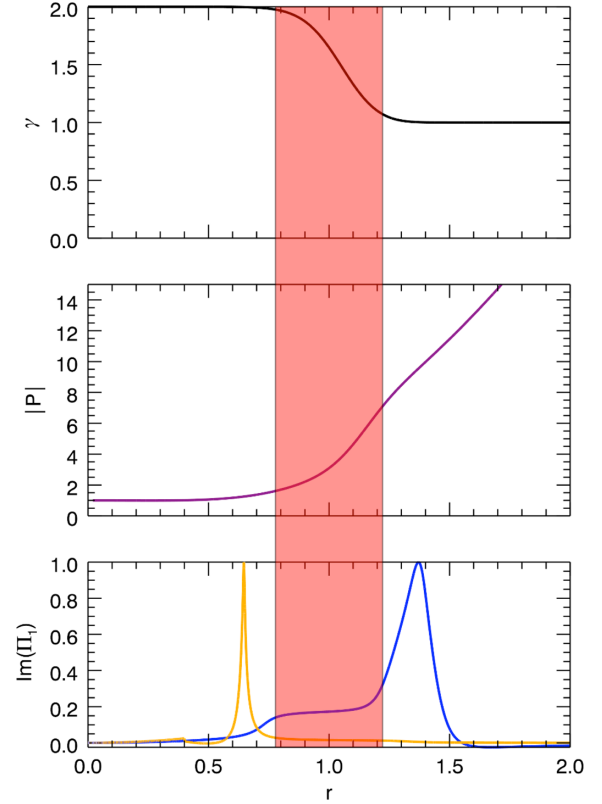

Figure 11. In the top panel we plot the profile of the Lorentz factor $\gamma(r)$, in the middle panel we plot the pitch profile $P(r)$ and in the bottom panel we plot the eigenfunctions for the inner (orange) and outer (blue) modes, for $\gamma_c = 2$, $P_c = 1$. The orange curve is for $k = 0.8$ (inner mode) and the blue curve is for $k = 0.1$ (outer mode).

where the primed quantities are measured in the jet frame, while the unprimed quantities are measured in the laboratory frame. From the scaling given by equation (36), we obtain

$$\mathrm{Im}(\omega) \sim \frac{\mathrm{Im}(\omega')}{\gamma_c} \sim \frac{P'^3_c}{\gamma_c} f\left(k' P'_c\right) \sim \frac{P^3_c}{\gamma^4_c} f(k P_c). \qquad (39)$$

The scaling of the growth rate with $1/\gamma^4_c$ is demonstrated by Fig. 12, where we plot $\mathrm{Im}(\omega) P^3_c \gamma^4_c$ as a function of the wavenumber for three different values of γ_c. The scaling is excellent around the maximum of the growth rate, where the eigenfunction is more concentrated in the jet core. As we move towards smaller values of k, the radial extension of the eigenfunction increases, the effect of the velocity shear becomes more important and the three curves deviate from one another. Besides, from equation (38), we have that $k P_c = k' P'_c$ and the stabilization condition in the laboratory frame can be also written as $k P_c = 1$. All the results presented so far have been obtained for $a/r_j = 0.6$. We recall that the value of the parameter a determines the width of the current distribution and we can then ask how the results depend on it. The width of the current distribution is related to the extent of the flat part in the pitch profile (see Fig. 2): thus, if we decrease a, the pitch grows to larger values inside the jet, the inner mode becomes stabilized at lower wavenumbers and the outer mode is also found at lower wavenumbers. The position of the stable region between the inner and outer branches is therefore a function of the value of a and moves towards smaller wavenumbers (when a is decreased) and to larger wavenumbers (when a is increased). In
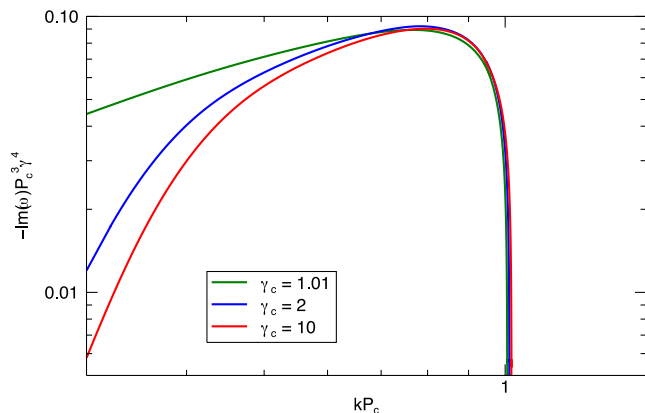
Figure 12. Plot of the growth rate as a function of the wavenumber for three different values of the Lorentz factor γ_c, as indicated in the legend. The values of P_c are chosen so that in the jet rest frame the pitch on the axis is equal to 2. The figure demonstrates the validity of the scaling of the growth rate with $1/\gamma_c^4$ close the maximum. For lower values of the wavenumber the curves deviate from the above scaling.
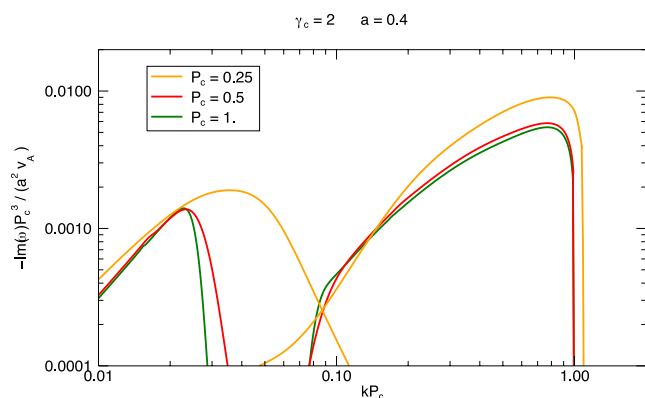
Figure 13. Plot of the growth rate as a function of the wavenumber, for the three different values of the pitch parameter P_c given in the legends and for $M_a = 0.01$ and $\gamma_c = 2$.

addition, the growth rate of the outer branch, being found at small values of k, decreases with a, while the growth rate of the inner branch is only determined by P_c and does not depend on a. We then expect that, by decreasing a, the inner mode will become dominant. As an example, we show in Fig. 13 how the results obtained for $a = 0.3$ confirm these expectations. The figure refers to $\gamma_c = 2$ and can be directly compared to the middle panel of Fig. 10.

We can now summarize the results obtained for the CDI in the relativistic regime: we have two branches of instability: an inner mode concentrated inside the jet and an outer mode in which the perturbation is concentrated outside the jet. The relative importance of the two branches depends both on the current concentration determined by the parameter a and on the Lorentz factor γ_c. In fact, as we decrease a, the growth rate of the outer branch also decreases and the mode shifts towards smaller wavenumbers, while the growth rate of the inner branch does not change. Conversely, as we increase γ_c, the growth rate of the inner branch decreases while the growth rate of the outer branch does not change.

5 SUMMARY

We have examined the stability properties of a relativistic magnetized cylindrical flow in the approximation of zero thermal pressure, neglecting also the effects of rotation and focusing only on the $|m| = 1$ mode. In this configuration we have two kinds of instability that may be present: Kelvin–Helmholtz (KH) and current driven. The instability behaviour depends of course on the chosen equilibrium configuration and this is somewhat arbitrary since we have no direct information on the magnetic field structure, although some indications are provided by the acceleration models (see e.g. Komissarov et al. 2007). Nevertheless, the general outcome and the properties of the solutions obtained for a particular configuration, such as the one we adopted here, can be considered valid for a more general class of equilibria. Our results can then be considered representative of an equilibrium configuration characterized by a distribution of current concentrated in the jet, with the return current assumed to be mainly found at very large distances.

We can summarize our results by considering the behaviour of the system for different values of the ratio between matter and magnetic energy densities. For matter-dominated flows, the dominant instability is KH and the wavenumber corresponding to the maximum growth rate as well as the growth rate itself scale both as $1/M_a v_c$. Somewhat above equipartition KHI reaches its maximum growth rate and then it becomes rapidly stabilized. Below this stabilization limit the dominant instability becomes CDI.

The dependence of the KHI on the value of the pitch is relatively weak and only for the smallest value of the axial pitch (P_c), in the relativistic case, we observe a displacement of the stability limit towards lower values of $M_a v_c$ and a merging with CDI. CDI are therefore prevailing for flows in equipartition or magnetically dominated and the dependence on $M_a v_c$ in these regimes is quite weak. The wavenumber corresponding to the maximum growth rate scales as $1/P_c$, the growth rate itself increases with decreasing P_c and the modes have a resonant character with a peak in the eigenfunction at the radial position where $kP(r) = 1$.

At low jet velocity, our equilibrium has no return current inside the domain, while at relativistic velocities we have a small portion of the return current corresponding to the velocity shear region. The corresponding steepening of the pitch profiles induces a stabilization of the modes for which the resonance condition corresponds to radial positions where the return current is found. We then observe a splitting of the CDI in two branches, one at high wavenumbers (the inner mode) characterized by an eigenfunction with a resonant peak in the inner radial part of the flow, and one at smaller wavenumbers (the outer mode) for which the resonant peak is outside the jet region. Which of the two branches is dominant depends on the width of the current distribution and on the Lorentz factor of the flow. An increase in the current concentration (small a) favours the growth of the inner mode, while an increase in γ_c enhances the development of the outer mode.

The different behaviour in the explored parameter ranges may have crucial implications for the non-linear stages as distinct types of instability may evolve differently. This study is therefore an essential first step for the interpretation of the results of numerical simulations that will be presented in a following paper and for their comparison with astrophysical data.

ACKNOWLEDGEMENT

REFERENCES

Appl S., 1996, A&A, 314, 995
Appl S., Camenzind M., 1992, A&A, 256, 354
Appl S., Lery T., Baty H., 2000, A&A, 355, 818
Baty H., Keppens R., 2002, ApJ, 580, 800
Begelman M. C., 1998, ApJ, 493, 291
Birkinshaw M., 1991, in Hughes P. A., ed., Beams and Jets in Astrophysics. Cambridge Univ. Press, Cmbridge, p. 278
Bodo G., Rosner R., Ferrari A., Knobloch E., 1989, ApJ, 341, 631
Bodo G., Rosner R., Ferrari A., Knobloch E., 1996, ApJ, 470, 797
Bonanno A., Urpin V., 2008, A&A, 488, 1
Bonanno A., Urpin V., 2011, Phys. Rev. E, 84, 056310
Celotti A., Ghisellini G., 2008, MNRAS, 385, 283
Ferrari A., Trussoni E., Zaninetti L., 1978, A&A, 64, 43
Hardee P. E., 1979, ApJ, 234, 47
Hardee P. E., 2006, in Hughes P. A., Bregman J. N., eds, AIP Conf. Ser. Vol. 856. Relativistic Jets: The Common Physics of AGN, Microquasars, and Gamma-Ray Bursts. AGN Jets: A Review of Stability and Structure. Am. Inst. Phys., New York, p. 57
Hardee P. E., Cooper M. A., Norman M. L., Stone J. M., 1992, ApJ, 399, 478

Istomin Y. N., Pariev V. I., 1994, MNRAS, 267, 629
Istomin Y. N., Pariev V. I., 1996, MNRAS, 281, 1
Komissarov S. S., Barkov M. V., Vlahakis N., Königl A., 2007, MNRAS, 380, 51
Lyubarskii Y. E., 1999, MNRAS, 308, 1006
McKinney J. C., Blandford R. D., 2009, MNRAS, 394, L126
Mignone A., Rossi P., Bodo G., Ferrari A., Massaglia S., 2010, MNRAS, 402, 7
Mizuno Y., Hardee P., Nishikawa K.-I., 2007, ApJ, 662, 835
Moll R., Spruit H. C., Obergaulinger M., 2008, A&A, 492, 621
Nakamura M., Meier D. L., 2004, ApJ, 617, 123
Narayan R., Li J., Tchekhovskoy A., 2009, ApJ, 697, 1681
Osmanov Z., Mignone A., Massaglia S., Bodo G., Ferrari A., 2008, A&A, 490, 493
Perucho M., Hanasz M., Martí J. M., Sol H., 2004, A&A, 427, 415
Perucho M., Martí J. M., Cela J. M., Hanasz M., de La Cruz R., Rubio F., 2010, A&A, 519, A41
Sikora M., Begelman M. C., Madejski G. M., Lasota J.-P., 2005, ApJ, 625, 72
Tomimatsu A., Matsuoka T., Takahashi M., 2001, Phys. Rev. D, 64, 123003
Urpin V., 2002, A&A, 385, 14

APPENDIX A: DERIVATION OF THE LINEARIZED EQUATIONS

We start from the linearized system (22–25) and, assuming the perturbations to be of the form $\propto \exp{(i\omega t - im\varphi - ikz)}$, rewriting the vectorial equations in components, substituting the condition $\nabla \cdot \boldsymbol{B}_1 = 0$ to the z component of the induction equation, we obtain the following mixed system of 11 differential and algebraic equations in the 11 unknowns ρ_1, v_{1r}, $v_{1\varphi}$, v_{1z}, B_{1r}, $B_{1\varphi}$, B_{1z}, E_{1r}, $E_{1\varphi}$, E_{1z}, Π_1, where we introduced the total electromagnetic pressure perturbation Π_1:

$$i\tilde{\omega}\frac{\rho_1}{\rho_0} + \frac{1}{r\rho_0\gamma_0}\frac{d}{dr}(r\rho_0\gamma_0 v_{1r}) + i\left(\tilde{\omega}\gamma_0^2 v_{0\varphi} - \frac{m}{r}\right)v_{1\varphi} + i\left(\tilde{\omega}\gamma_0^2 v_{0z} - k\right)v_{1z} = 0. \tag{A1}$$

$$i\omega\rho_0\gamma_0^2 v_{1r} - \frac{2\rho_0\gamma_0^2 v_{0\varphi}}{r}\left(\gamma_0^2 v_{0\varphi}^2 + 1\right)v_{1\varphi} - \frac{2\rho_0\gamma_0^4 v_{0\varphi}^2 v_{0z}}{r}v_{1z} - \frac{\gamma_0^2 v_{0\varphi}^2}{r}\rho_1 = -\frac{d\Pi_1}{dr} - \frac{2\Pi_1}{r} + \frac{2B_{0z}B_{1z}}{r} - i\overline{\omega}B_{0z}E_{1\varphi} - ik_B B_{1r}$$
$$+ i\Omega rk B_{0z}E_{1z} + i\omega B_{0\varphi}E_{1z}, \tag{A2}$$

$$i\tilde{\omega}\rho_0\gamma_0^2\left(\gamma_0^2 v_{0\varphi}^2 + 1\right)v_{1\varphi} + i\tilde{\omega}\rho_0\gamma_0^4 v_{0\varphi}v_{0z}v_{1z} + \frac{\gamma_0\rho_0 v_{1r}}{r}\frac{d}{dr}(r\gamma_0 v_{0\varphi}) = \frac{B_{1r}}{r}\frac{d}{dr}(rB_{0\varphi}) + \frac{im}{r}B_{0z}B_{1z} - ik B_{0z}B_{1\varphi} + i\omega B_{0z}E_{1r} + \frac{E_{1\varphi}}{r}\frac{d}{dr}(rE_{0r}) \tag{A3}$$

$$i\tilde{\omega}\rho_0\gamma_0^2\left(\gamma_0^2 v_{0z}^2 + 1\right)v_{1z} + i\tilde{\omega}\rho_0\gamma_0^4 v_{0\varphi}v_{0z}v_{1\varphi} + \rho_0\gamma_0 v_{1r}\frac{d}{dr}(\gamma_0 v_{0z}) = B_{1r}\frac{dB_{0z}}{dr} - \frac{im}{r}B_{0\varphi}B_{1z} + ik B_{0\varphi}B_{1\varphi} - i\omega B_{0\varphi}E_{1r} + \frac{E_{1z}}{r}\frac{d}{dr}(rE_{0r}). \tag{A4}$$

$$\omega B_{1r} = \frac{m}{r}E_{1z} - kE_{1\varphi}, \tag{A5}$$

$$i\omega B_{1\varphi} = \frac{dE_{1z}}{dr} + ik E_{1r} \tag{A6}$$

$$\frac{1}{r}\frac{d}{dr}(rB_{1r}) - \frac{im}{r}B_{1\varphi} - ik B_{1z} = 0. \tag{A7}$$

$$E_{1r} = B_{0\varphi}v_{1z} - B_{0z}v_{1\varphi} + v_{0z}B_{1\varphi} - v_{0\varphi}B_{1z} \tag{A8}$$

$$E_{1\varphi} = v_{1r}B_{0z} - v_{0z}B_{1r} \tag{A9}$$

$$E_{1z} = -v_{1r}B_{0\varphi} + v_{0\varphi}B_{1r}. \tag{A10}$$

$$\Pi_1 = \boldsymbol{B}_0 \cdot \boldsymbol{B}_1 - \boldsymbol{E}_0 \cdot \boldsymbol{E}_1 = B_{0\varphi}B_{1\varphi} + B_{0z}B_{1z} - E_{0r}E_{1r} \tag{A11}$$

where we defined

$$\bar{\omega} \equiv \omega - m\Omega, \quad k_B \equiv \frac{m}{r}B_{0\varphi} + kB_{0z}, \quad \tilde{\omega} \equiv \omega - \frac{m}{r}v_{0\varphi} - kv_{0z} = \bar{\omega} - \kappa k_B, \tag{A12}$$

Furthermore, following Istomin & Pariev (1996), it is convenient to introduce the radial displacement of fluid elements, $\xi_{1r} = -iv_{1r}/\tilde{\omega}$ and use it instead of v_{1r}. We will now try to express all the variable in terms of ξ_{1r} and Π_1 and substitute them in equations (A2) and (A7) obtaining a system of two first order differential equations in the two unknowns ξ_{1r} and Π_1.

From equations (A5), (A9) and (A10), we solve for B_{1r}, $E_{1\varphi}$ and E_{1z} in terms of ξ_{1r}

$$B_{1r} = -ik_B\xi_{1r} \tag{A13}$$

$$E_{1\varphi} = i\bar{\omega}B_{0z}\xi_{1r} \tag{A14}$$

$$E_{1z} = -i\left(\Omega k_B r + \bar{\omega}B_{0\varphi}\right)\xi_{1r}. \tag{A15}$$

For further use it is convenient to define the velocity components parallel and transversal to the background magnetic field

$$u_{1\parallel} = B_{0\varphi}v_{1\varphi} + B_{0z}v_{1z}, \quad v_{1\varphi} = \frac{B_{0\varphi}}{B_0^2}u_{1\parallel} - \frac{B_{0z}}{B_0^2}u_{1\perp} \tag{A16}$$

$$u_{1\perp} = B_{0\varphi}v_{1z} - B_{0z}v_{1\varphi}, \quad v_{1z} = \frac{B_{0z}}{B_0^2}u_{1\parallel} + \frac{B_{0\varphi}}{B_0^2}u_{1\perp}, \tag{A17}$$

where $B_0^2 = B_{0\varphi}^2 + B_{0z}^2$.

Substituting E_{1z} from equation (A15) and E_{1r} from (A8) into equation (A6) and eliminating the radial derivative dB_{1r}/dr from equation (A7), we get

$$k_B u_{1\perp} - \tilde{\omega}B_{0z}B_{1\varphi} + \tilde{\omega}B_{0\varphi}B_{1z} = FB_{0z}\xi_{1r}, \tag{A18}$$

where

$$F \equiv rk_B\frac{d\Omega}{dr} + \bar{\omega}\left(\frac{dB_{0\varphi}}{dr} - \frac{B_{0\varphi}}{r} - \frac{B_{0\varphi}}{B_{0z}}\frac{dB_{0z}}{dr}\right).$$

A second relation comes from the definition of the electromagnetic pressure, Π_1, equation (A11), if we substitute into it $E_{0r} = -\Omega r B_{0z}$ and E_{1r} from equation (A8):

$$\Omega r B_{0z}u_{1\perp} + (B_{0\varphi} + \Omega r B_{0z}v_{0z})B_{1\varphi} + B_{0z}(1 - \Omega r v_{0\varphi})B_{1z} = \Pi_1. \tag{A19}$$

Now expressing $v_{1\varphi}$ and v_{1z} through $u_{1\parallel}$ and $u_{1\perp}$ from equations (A16) and (A17), substituting into equations (A3) and (A4) and then eliminating $u_{1\parallel}$, we get the third relation:

$$\tilde{\omega}Yu_{1\perp} + \sigma(k - \omega v_{0z})B_{1\varphi} + \sigma\left(\omega v_{0\varphi} - \frac{m}{r}\right)B_{1z} = G\xi_{1r}, \tag{A20}$$

where

$$\sigma = \frac{B_0^2}{\rho_0\gamma_0^2}, \quad Y = -\frac{\omega}{\tilde{\omega}}\sigma - \frac{B_0^2}{B_0^2 - E_0^2}, \quad G = W - \frac{\tilde{\omega}E_0(\mathbf{v}_0\cdot\mathbf{B}_0)}{B_0^2 - E_0^2}H$$

$$H = \frac{1}{\gamma_0}\left(B_{0\varphi}\frac{d}{dr}(\gamma_0 v_{0\varphi}) + B_{0z}\frac{d}{dr}(\gamma_0 v_{0z}) + \frac{\gamma_0 B_{0\varphi}v_{0\varphi}}{r}\right) + \frac{k_B v_{0\varphi}^2}{r\tilde{\omega}}$$

$$W = \frac{\tilde{\omega}}{\gamma_0}\left(B_{0\varphi}\frac{d}{dr}(\gamma_0 v_{0z}) - B_{0z}\frac{d}{dr}(\gamma_0 v_{0\varphi}) - \frac{\gamma_0 B_{0z}v_{0\varphi}}{r}\right)$$

$$+ \sigma\left[(\nabla\cdot\mathbf{E}_0)\left(\bar{\omega} + \frac{\Omega r B_{0\varphi}k_B}{B_0^2}\right) - \frac{\mathbf{J}_0\cdot\mathbf{B}_0}{B_0^2}k_B\right].$$

Equations (A18), (A19) and (A20) form a system of three linear equations

$$k_B u_{1\perp} - \tilde{\omega}B_{0z}B_{1\varphi} + \tilde{\omega}B_{0\varphi}B_{1z} = FB_{0z}\xi_{1r},$$

$$\Omega r B_{0z}u_{1\perp} + (B_{0\varphi} + \Omega r B_{0z}v_{0z})B_{1\varphi} + B_{0z}(1 - \Omega r v_{0\varphi})B_{1z} = \Pi_1$$

$$\tilde{\omega}Yu_{1\perp} + \sigma(k - \omega v_{0z})B_{1\varphi} + \sigma\left(\omega v_{0\varphi} - \frac{m}{r}\right)B_{1z} = G\xi_{1r}, \tag{A21}$$

from which one can solve for $u_\perp$, $B_{1\varphi}$ and B_{1z} in terms of ξ_{1r} and Π_1. The solubility of this system depends on the determinant of the left-hand side

$$D = \begin{vmatrix} k_B & -\tilde\omega B_{0z} & \tilde\omega B_{0\varphi} \\ \Omega r B_{0z} & (B_{0\varphi} + \Omega r B_{0z} v_{0z}) & B_{0z}(1 - \Omega r v_{0\varphi}) \\ \tilde\omega Y & \sigma(k - \omega v_{0z}) & \sigma\left(\omega v_{0\varphi} - \frac{m}{r}\right) \end{vmatrix},$$ (A22)

which after simplification reduces to

$$D = (\sigma + 1)B_0^2 \tilde\omega^2 + \sigma k_B \left[2\tilde\omega(\boldsymbol{v}_0 \cdot \boldsymbol{B}_0) - \frac{k_B}{\gamma_0^2}\right].$$ (A23)

The possible singularities deriving from this determinant are discussed in the main text in Section 3. At this point we are able to express all the variables in terms of ξ_{1r}, Π_1 [in particular for expressing ρ_1 we make use of equation (A1)], and substituting them into equations (A2) and (A7) after a long but straightforward algebra, we arrive at the system of two first order differential equations in the radial coordinate for the two basic variables – the radial displacement and the perturbed electromagnetic pressure:

$$D\frac{d\xi_{1r}}{dr} = \left(C_1 + \frac{C_2 - Dk'_B}{k_B} - \frac{D}{r}\right)\xi_{1r} - C_3\Pi_1$$ (A24)

$$D\frac{d\Pi_1}{dr} = \left[A_1 D - \frac{\rho_0\gamma_0^2 v_{0\varphi}^2}{r}\left(C_1 + \frac{C_2 - Dk'_B}{k_B}\right)\right]\xi_{1r} + \frac{1}{r}\left(\rho_0\gamma_0^2 v_{0\varphi}^2 C_3 - 2D\right)\Pi_1 + \frac{2B_{0z}}{r}DB_{1z} + A_2 Du_{1\perp}$$ (A25)

where $k'_B \equiv dk_B/dr$ and the long expressions for A_1, A_2, C_1, C_2, C_3 and for $Du_{1\perp}$, DB_{1z} through ξ_{1r}, Π_1 are given in Appendix B.

APPENDIX B: COEFFICIENTS OF THE LINEAR SYSTEM

$$A_1 \equiv \bar\omega^2 B_0^2 + \Omega^2 r^2 k_B^2 + 2\bar\omega B_{0\varphi}\Omega r k_B - k_B^2 + \rho_0\gamma_0^2\tilde\omega^2 - \frac{\gamma_0 v_{0\varphi}^2}{r\tilde\omega}\frac{d}{dr}(\gamma_0\rho_0\tilde\omega) - \frac{\rho_0 v_{0\varphi}H}{r(B_0^2 - E_0^2)}\left(2B_{0\varphi} + \gamma_0^2 v_{0\varphi}(\boldsymbol{v}_0 \cdot \boldsymbol{B}_0) + \frac{v_{0\varphi}k_B}{\tilde\omega}\right),$$ (B1)

$$A_2 \equiv \frac{\rho_0\gamma_0^2 v_{0\varphi}}{rB_0^2}\left[\frac{v_{0\varphi}}{\tilde\omega}\left(kB_{0\varphi} - \frac{m}{r}B_{0z}\right) - 2B_{0z} + \frac{E_0 v_{0\varphi}B_0^2}{B_0^2 - E_0^2} - \frac{E_0(\boldsymbol{v}_0 \cdot \boldsymbol{B}_0)}{B_0^2 - E_0^2}\left(2B_{0\varphi} + \frac{v_{0\varphi}k_B}{\tilde\omega}\right)\right],$$ (B2)

$$C_1 \equiv G\left(\frac{m}{r}B_{0z} - kB_{0\varphi} - \Omega r B_{0z}\omega\right) - \frac{F\tilde\omega B_0^2 \Omega r v_{0z}B_{0z}}{B_0^2 - E_0^2},$$ (B3)

$$C_2 \equiv FB_{0z}\left[\left(\frac{m}{r}B_{0z} - kB_{0\varphi}\right)\left(\omega\sigma + \frac{\tilde\omega B_0^2}{B_0^2 - E_0^2}\right) - \sigma\Omega r B_{0z}\left(k^2 + \frac{m^2}{r^2}\right) - \frac{mr\tilde\omega B_{0z}B_0^2\Omega^2}{B_0^2 - E_0^2}\right],$$ (B4)

$$C_3 \equiv \sigma\left(\omega^2 - \frac{m^2}{r^2} - k^2\right) + \frac{\tilde\omega^2 B_0^2}{B_0^2 - E_0^2}$$ (B5)

and $u_{1\perp}$ and B_{1z} expressed through ξ_{1r} and Π_1 are

$$Du_{1\perp} = \left[\sigma B_{0z}F\left(\tilde\omega(\boldsymbol{v}_0 \cdot \boldsymbol{B}_0) - \frac{k_B}{\gamma_0^2}\right) - G\tilde\omega(B_0^2 - E_0^2)\right]\xi_{1r} + \sigma\tilde\omega\left(kB_{0\varphi} - \frac{m}{r}B_{0z} + \omega\Omega r B_{0z}\right)\Pi_1,$$ (B6)

$$DB_{1z} = \left[G(k_B B_{0\varphi} - \bar\omega E_0 B_{0z}) + FB_{0z}\left(\omega\sigma B_{0\varphi} + \sigma\Omega r B_{0z}k + \frac{\tilde\omega B_0^2(B_{0\varphi} + \Omega r B_{0z}v_{0z})}{B_0^2 - E_0^2}\right)\right]\xi_{1r} + \left[\sigma(\omega\bar\omega B_{0z} - kk_B) + \frac{\tilde\omega^2 B_0^2 B_{0z}}{B_0^2 - E_0^2}\right]\Pi_1,$$ (B7)

where D is the determinant (A23).

The second equation (A25), after expressing DB_{1z} and $Du_{1\perp}$ through ξ_{1r} and Π_1, takes the form

$$D\frac{d\Pi_1}{dr} = \left[A_1 D - \frac{\rho_0\gamma_0^2 v_{0\varphi}^2}{r}\left(C_1 + \frac{C_2 - Dk'_B}{k_B}\right) + \frac{C_4}{r} + C_5\right]\xi_{1r} + \left[\frac{1}{r}\left(\rho_0\gamma_0^2 v_{0\varphi}^2 C_3 - 2D + C_6\right) + C_7\right]\Pi_1,$$ (B8)

where the coefficients C_4, C_5, C_6, C_7 are given by

$$C_4 = 2B_{0z}G(k_B B_{0\varphi} - \bar\omega E_0 B_{0z}) + 2FB_{0z}^2\left(\omega\sigma B_{0\varphi} + \sigma\Omega r B_{0z}k + \frac{\tilde\omega B_0^2(B_{0\varphi} + \Omega r B_{0z}v_{0z})}{B_0^2 - E_0^2}\right),$$

$$C_5 = A_2 \left[\sigma B_{0z} F \left(\tilde{\omega}(\boldsymbol{v}_0 \cdot \boldsymbol{B}_0) - \frac{k_B}{\gamma_0^2} \right) - G\tilde{\omega}(B_0^2 - E_0^2) \right]$$

$$C_6 = 2B_{0z}\sigma(\omega\tilde{\omega}B_{0z} - kk_B) + \frac{2\tilde{\omega}^2 B_0^2 B_{0z}^2}{B_0^2 - E_0^2}$$

$$C_7 = A_2\sigma\tilde{\omega} \left(kB_{0\varphi} - \frac{m}{r} B_{0z} + \omega\Omega r B_{0z} \right).$$

APPENDIX C: ASYMPTOTIC SOLUTION AT SMALL RADII

To find the solution of equations (28) and (29) at small radii, we calculate the coefficients entering these equations at $r \to 0$ taking into account that in this limit the equilibrium quantities $v_{0\varphi}, B_{0\varphi} \propto r$, while v_{0z} and B_{0z} tend to constant values. Thus we have (primes everywhere denote radial derivative)

$$\lim_{r \to 0} k_B = kB_{0z} + mB'_{0\varphi}, \quad \lim_{r \to 0} k'_B = kB'_{0z},$$

$$\lim_{r \to 0} D = B_{0z}^2\tilde{\omega}^2 + \sigma(\overline{\omega}^2 B_{0z}^2 - k_B^2)$$

$$\lim_{r \to 0} A_1 = \overline{\omega}^2 B_{0z}^2 - k_B^2 + \rho_0\gamma_0^2\tilde{\omega}^2, \quad \lim_{r \to 0} A_2 = -\frac{\rho_0\gamma_0^2 v'_{0\varphi}}{B_{0z}} \left(\frac{mv'_{0\varphi}}{\tilde{\omega}} + 2 \right)$$

$$\lim_{r \to 0} C_1 = -\frac{2m B_{0z}^2}{r} \left(\tilde{\omega}v'_{0\varphi} + \sigma\overline{\omega}\Omega + \frac{\sigma B'_{0\varphi}k_B}{B_{0z}^2} \right)$$

$$\lim_{r \to 0} C_2 = m B_{0z}^2 \left[k_B \frac{d\Omega}{dr} + \overline{\omega} \left(\frac{B''_{0\varphi}}{2} - \frac{B'_{0\varphi}}{B_{0z}} \frac{dB_{0z}}{dr} \right) \right] (\sigma\overline{\omega} + \tilde{\omega})$$

$$\lim_{r \to 0} C_3 = -\sigma\frac{m^2}{r^2}$$

$$\lim_{r \to 0} Du_{1\perp} = 2\tilde{\omega}B_{0z}^3 \left(\tilde{\omega}v'_{0\varphi} + \sigma\overline{\omega}\Omega + \frac{\sigma B'_{0\varphi}k_B}{B_{0z}^2} \right) \xi_{1r} - \tilde{\omega}m\sigma B_{0z} \frac{\Pi_1}{r}$$

$$\lim_{r \to 0} DB_{1z} = -2B_{0z}(k_B B'_{0\varphi} + \overline{\omega}\Omega B_{0z}^2) \left(\tilde{\omega}v'_{0\varphi} + \sigma\Omega\overline{\omega} + \frac{\sigma B'_{0\varphi}k_B}{B_0^2} \right) \xi_{1r} + [\sigma(\omega\overline{\omega}B_{0z} - kk_B) + \tilde{\omega}^2 B_{0z}]\Pi_1.$$

Substituting these coefficients into equations (28) and (29), to leading order, we obtain

$$\frac{d\xi_{1r}}{dr} = -\frac{1}{r} \left[1 + \frac{2m B_{0z}^2}{D} \left(\tilde{\omega}v'_{0\varphi} + \sigma\overline{\omega}\Omega + \frac{\sigma B'_{0\varphi}k_B}{B_{0z}^2} \right) \right] \xi_{1r} + \frac{m^2\sigma}{r^2 D} \Pi_1, \tag{C1}$$

$$\frac{d\Pi_1}{dr} = \frac{2m B_{0z}^2}{rD} \left(\tilde{\omega}v'_{0\varphi} + \sigma\overline{\omega}\Omega + \frac{\sigma B'_{0\varphi}k_B}{B_{0z}^2} \right) \Pi_1 + \frac{D}{\sigma} \left[1 - \frac{4B_{0z}^4}{D^2} \left(\tilde{\omega}v'_{0\varphi} + \sigma\overline{\omega}\Omega + \frac{\sigma B'_{0\varphi}k_B}{B_{0z}^2} \right)^2 \right] \xi_{1r}. \tag{C2}$$

We look for solutions in the form $\xi_{1r} \propto r^\alpha$, $\Pi_1 \propto r^{\alpha+1}$. After substitution of this form into equations (C1) and (C2) we get

$$\alpha = \pm|m| - 1,$$

but because a solution must be regular at $r = 0$ we take only $\alpha = |m| - 1$, $(|m| \geq 1)$, and after that the ratio

$$\frac{\Pi_1}{\xi_{1r}} = \frac{r}{m\sigma} \left[\text{sign}(m)D + 2B_{0z}^2 \left(\tilde{\omega}v'_{0\varphi} + \sigma\overline{\omega}\Omega + \frac{\sigma B'_{0\varphi}k_B}{B_{0z}^2} \right) \right]_{|r=0}. \tag{C3}$$

This equation together with the choice $\alpha = |m| - 1$ serves as our boundary condition at small radii.

APPENDIX D: ASYMPTOTIC SOLUTION AT LARGE RADII

To find the asymptotic limit of equations (28) and (29) and their corresponding solutions at large radii, we notice that the equilibrium azimuthal velocity, $v_{0\varphi}$, the vertical velocity v_{0z} and Ω decay very quickly (exponentially) with radius according to equations (8), (13), (15)

and (17)), so we can put them effectively zero, $v_{0\varphi} \simeq 0$, $v_{0z} \simeq 0$, $\Omega \simeq 0$ at large radii and hence $\gamma_0 = 1$. At large r, the equilibrium density and vertical magnetic field are constant, while the azimuthal magnetic field falls off as $B_{0\varphi} \propto 1/r$, as follows from equations (12), (15), (16) and (18). Taking this into account, the asymptotic form of each coefficient entering equations (28) and (29) was calculated at large $r \to \infty$. Then, neglecting everywhere terms of the order of $O(r^{-3})$ and higher, after a rather lengthy algebra, we arrive at the following second order differential equation for the total electromagnetic pressure perturbation Π_1

$$\frac{d^2 \Pi_1}{dr^2} + \frac{1}{r}\frac{d\Pi_1}{dr} + \left[\frac{\rho_0 + B_{0z}^2}{B_{0z}^2}\omega^2 - k^2 - \left(m^2 + \frac{\rho_0 B_{\varphi c}^2 \omega^2}{B_{0z}^4} \right)\frac{1}{r^2} \right]\Pi_1 = 0, \tag{D1}$$

which is of Bessel's equation type. Its solution corresponding to radially propagating waves that vanish at infinity is the Hankel function of the first kind $\Pi_1 = H_\nu^{(1)}(\chi r)$, where

$$\chi^2 = \frac{\rho_0 + B_{0z}^2}{B_{0z}^2}\omega^2 - k^2, \quad \nu^2 = m^2 + \frac{\rho_0 B_{\varphi c}^2 \omega^2}{B_{0z}^4},$$

with the leading term of the asymptotic expansion at $r \to \infty$

$$\Pi_1 = H_\nu^{(1)}(\chi r) \simeq \sqrt{\frac{2}{\pi \chi r}} \exp\left[i\left(\chi r - \frac{\nu\pi}{2} - \frac{\pi}{4} \right) \right]. \tag{D2}$$

The complex parameter χ can have either positive or negative sign,

$$\chi = \pm\sqrt{\frac{\rho_0 + B_{0z}^2}{B_{0z}^2}\omega^2 - k^2}.$$

Requiring that the perturbations decay at large radii, we choose the root of χ^2 in equation (D2) that has a positive imaginary part, $\mathrm{Im}(\chi) > 0$. These perturbations are produced within the jet and hence at large radii should have the character of radially outgoing waves. This implies that the real parts of χ and ω should have opposite signs, $\mathrm{Re}(\omega)\,\mathrm{Re}(\chi) < 0$ (Sommerfeld condition), in order to give the phase velocity directed outwards from the jet.

The asymptotic behaviour of the displacement ξ_{1r} can be readily obtained from Π_1 again correct to $O(r^{-3})$

$$\xi_{1r} = \frac{\Pi_1}{\omega^2(\rho_0 + B_0^2) - k_B^2}\left(i\chi - \frac{1}{2r} \right). \tag{D3}$$

The asymptotic solutions (D2) and (D3), together with the above requirements of outgoing waves with decaying amplitudes at $r \to \infty$, are used as an initial condition at outer jet boundary in our numerical scheme for finding eigenvalues of ω, when doing integration backwards, from large to small radii.

This paper has been typeset from a TₑX/LATₑX file prepared by the author.